Regolith-atmosphere exchange of water in Mars' recent past

Regolith-atmosphere exchange of water in Mars' recent past

Liam J. Steele[a,*], Matthew R. Balme[a], Stephen R. Lewis[a]

[a]*Department of Physical Sciences, The Open University, Walton Hall, Milton Keynes MK7 6AA, United Kingdom*

Abstract

We investigate the exchange of water vapour between the regolith and atmosphere of Mars, and how it varies with different orbital parameters, atmospheric dust contents and surface water ice reservoirs. This is achieved through the coupling of a global circulation model (GCM) and a regolith diffusion model. GCM simulations are performed for hundreds of Mars years, with additional one-dimensional simulations performed for 50 kyr. At obliquities $\varepsilon = 15°$ and 30°, the thermal inertia and albedo of the regolith have more control on the subsurface water distribution than changes to the eccentricity or solar longitude of perihelion. At $\varepsilon = 45°$, atmospheric water vapour abundances become much larger, allowing stable subsurface ice to form in the tropics and mid-latitudes. The circulation of the atmosphere is important in producing the subsurface water distribution, with increased water content in various locations due to vapour transport by topographically-steered flows and stationary waves. As these circulation patterns are due to topographic features, it is likely the same regions will also experience locally large amounts of subsurface water at different epochs. The dustiness of the atmosphere plays an important role in the distribution of subsurface water, with a dusty atmosphere resulting in a wetter water cycle and increased stability of subsurface ice deposits.

Keywords: Mars, Mars, atmosphere, Mars, climate, Mars, surface

*Corresponding author. Tel: +44(0)1908 659877.
Email address: liam.steele@open.ac.uk (Liam J. Steele)

1. Introduction

Studies of possible regolith-atmosphere exchange of water on Mars date back many years (e.g. Smoluchowski, 1968; Flasar and Goody, 1976; Fanale and Jakosky, 1982; Fanale et al., 1986; Clifford, 1993; Mellon and Jakosky, 1993; Mellon et al., 1997), but it was not until observations by the Gamma Ray Spectrometer (GRS) suite of instruments aboard Mars Odyssey that the presence of large subsurface reservoirs of water was revealed (Boynton et al., 2002; Feldman et al., 2004, 2007, 2008; Maurice et al., 2011). Since this time, additional observations of water from the surface have been made by the Phoenix lander (Mellon et al., 2009; Cull et al., 2010). The trenches dug by the Phoenix lander exposed ice at a mean depth of 4.6 cm, with the ice found to be mostly pore ice, though thin and relatively pure ice deposits were also observed near the surface (Mellon et al., 2009). Observations using the ChemCam instrument on the Curiosity rover have revealed a hydrogen emission peak in some soils, which may be the result of adsorbed water or hydration of the amorphous component of the soil (Meslin et al., 2013). New impact craters have revealed evidence for relatively pure subsurface ice in the mid-latitudes (Byrne et al., 2009).

In order to understand the regolith-atmosphere exchange of water, and determine the origin of the observed water distribution, numerous laboratory experiments and modelling studies have been undertaken. Laboratory studies have focused on calculating the diffusion coefficient of water vapour in the regolith, and the adsorption of water onto regolith grains (Zent and Quinn, 1997; Chevrier et al., 2007; Hudson et al., 2007; Bryson et al., 2008; Chevrier et al., 2008; Hudson and Aharonson, 2008; Sizemore and Mellon, 2008; Beck et al., 2010; Siegler et al., 2012). As well as revealing information on likely rates of diffusion and ice stability in different materials at different conditions, these studies also provide useful constraints for models of regolith-atmosphere interaction.

Previous modelling studies have focused on understanding the subsurface water distribution and the stability of subsurface ice in both the past and present epochs. These studies involve either (i) the explicit calculation of water vapour diffusion between the regolith and atmosphere (Mellon and Jakosky, 1993; Tokano, 2003; Böttger et al., 2005; Schorghofer and Aharonson, 2005; Schorghofer, 2007; Schorghofer and Forget, 2012; Williams et al., 2015), or (ii) the determination of the equilibrium ice table depth from subsurface temperatures and near-surface water vapour values (Mellon and

Jakosky, 1995; Mellon et al., 1997, 2004; Aharonson and Schorghofer, 2006; Chamberlain and Boynton, 2007; Zent, 2008).

For present-day conditions, studies find that subsurface ice is mostly stable polewards of $\pm 50°$, with the regolith thermal inertia and albedo playing a role in the stability of subsurface ice, in agreement with the GRS observations (Mellon and Jakosky, 1993; Mellon et al., 1997, 2004; Tokano, 2003; Böttger et al., 2005; Schorghofer and Aharonson, 2005; Aharonson and Schorghofer, 2006; Chamberlain and Boynton, 2007). The mid-latitudes are largely ice free, though regions with high surface roughness may contain detectable quantities of ice (Aharonson and Schorghofer, 2006), while shallow subsurface ice is required to account for the distribution of CO_2 ice on pole-facing slopes in the southern mid-latitudes (Vincendon et al., 2010). The formation of ice lenses has been investigated in order to understand the Phoenix observations of shallow, relatively pure water ice that cannot be explained by vapour diffusion alone (Sizemore et al., 2015), and it has been proposed that some subsurface ice in the present day may be the remnants of buried surface ice deposits from a past climate (e.g. Jakosky and Carr, 1985; Mischna et al., 2003; Levrard et al., 2004).

For past epochs, studies have focused on determining the equilibrium ice table depth, and how it varies with orbital parameters (Mellon and Jakosky, 1995; Chamberlain and Boynton, 2007; Zent, 2008), and the time integration of the subsurface ice content in a model initialized with an ice sheet (Schorghofer, 2007; Schorghofer and Forget, 2012). Unlike the present study, these simulations do not consider the feedback between the subsurface water content and the global circulation, and are instead run as one-dimensional models for specific locations on the surface (Mellon and Jakosky, 1995; Chamberlain and Boynton, 2007; Zent, 2008), or consider zonal averages (Schorghofer, 2007; Schorghofer and Forget, 2012). Additionally, the simulations of Mellon and Jakosky (1995), Schorghofer (2007) and Schorghofer and Forget (2012) were run for thousands or millions of years, and as they are interested in the long-term behaviour of subsurface water, large time steps are used. Mellon and Jakosky (1995) use time steps of 5 minutes for the thermal model and 10 sols for the diffusion model, while Schorghofer (2007) and Schorghofer and Forget (2012) use time steps of 30 minutes for the thermal model and 100–250 years for changes in subsurface ice content. Because of the one-dimensional nature of the models, various assumptions are made, such as how the atmospheric water content and pressure vary in past epochs, which will affect the diffusion calculation.

In this paper we investigate how the regolith-atmosphere interaction of water vapour via diffusion varies with different orbital parameters, atmospheric dust contents and surface ice reservoirs. We use a global circulation model (GCM) coupled with a regolith diffusion model, and run simulations for hundreds of Mars years. This removes the need to make assumptions about the near-surface atmospheric water content, and allows us to study the spatial distribution of subsurface water over the whole globe, and how it is affected by the atmospheric circulation. One-dimensional studies using the GCM output are also performed over longer time periods (50 kyr) for various locations at different obliquities.

2. Model description

2.1. Global circulation model

The GCM used for this study results from collaboration between the Laboratoire de Météorologie Dynamique (LMD), the University of Oxford and The Open University. The model combines the most recent LMD physical schemes with a spectral dynamical core, an energy and angular-momentum conserving vertical finite-difference scheme and a semi-Lagrangian advection scheme for tracers (for further details see Forget et al., 1999; Lewis et al., 2007). For the surface properties, we use data from the Thermal Emission Spectrometer (TES). Albedos are from Christensen et al. (2001), while thermal inertias are from Mellon et al. (2000), with corrections made to account for the effect of clouds in the initial dataset (Wilson et al., 2007). Small-scale topographic parameters used by the gravity wave drag scheme, along with the resolved topography, are obtained from MOLA data (Zuber et al., 1992; Smith et al., 1998). These data are stored as $1^\circ \times 1^\circ$ global maps, which are smoothed to the required model resolution.

Due to the spectral nature of the model, different resolutions are referenced using the label Tx, where 'T' represents triangular spectral truncation, and x represents the horizontal wavenumber the model is truncated at. The results presented in this paper are obtained using two different model resolutions. To enable study of the global regolith-atmosphere interaction over many hundreds of Mars years, the majority of simulations are run at T5 spectral truncation, which corresponds to a grid resolution of 22.5° in latitude and longitude for physical processes. Test simulations using present-day conditions were compared to observations and previous modelling studies (e.g. Smith, 2004; Navarro et al., 2014; Steele et al., 2014b) which showed that

the T5 resolution could reproduce the present-day water cycle (see section 4). Additional simulations are performed at T31 spectral truncation (5° resolution) to gain a better understanding of the spatial distribution and stability of surface and subsurface ice. In the vertical there are 20 levels in sigma coordinates, extending to an altitude of ∼85 km.

Dust is not transported in the model because of the difficulty in accounting for surface lifting at low resolutions. Instead, we set the global visible dust optical depth, $\tau_{\rm vis}$, to either 0.3 or 3, in order to account for both clear and dusty conditions (these values are comparable to the optical depths observed in the present day during clear periods and global dust storms respectively). The vertical profile of dust follows a modified Conrath distribution (Lewis et al., 1999), with the altitude of the dust top being dependent on the dustiness of the atmosphere. For the clear simulations ($\tau_{\rm vis} = 0.3$) the dust top is taken to be $z_{\rm top} = 30$ km, while for the dusty simulations ($\tau_{\rm vis} = 3$) we set $z_{\rm top} = 60$ km. These values are in agreement with present-day observations (e.g. Määttänen et al., 2013; Smith et al., 2013).

Water vapour and ice mass mixing ratios are transported as tracers, using the microphysics scheme of Montmessin et al. (2004) to account for the formation and sedimentation of ice particles. Clouds in the model are not radiatively active. While it has been shown that clouds in the present-day climate can influence the temperature structure of the atmosphere and strengthen the overturning circulation (e.g. Wilson et al., 2008; Madeleine et al., 2012; Steele et al., 2014a; Navarro et al., 2014), their inclusion in models has also led to some inconsistencies compared with spacecraft observations. Additionally, as we are not transporting dust we cannot account for the complex coupling between the dust and water cycles (e.g. Kahre et al., 2015). Ice can sediment anywhere on the surface, and if more than 5 pr-μm of water ice is deposited onto the surface, the albedo is changed from that of the regolith (derived from TES data) to that of water ice (0.4). Surface water ice can only sublime if there is no covering layer of CO_2 ice.

2.2. Regolith model

The regolith model is an updated version of that used by Böttger et al. (2004, 2005), which is based on the one-dimensional model of Zent et al. (1993). Diffusion is calculated implicitly on 30 unevenly-spaced levels extending to around 20 m below the surface. (The first four levels are within 1 mm of the surface, with the first level at 0.1 mm.) While the GCMs physical

time step is 30 minutes (used for calculating radiative transfer, tracer transport, turbulence, convection etc.), the regolith model operates on a shorter time step of 1 minute. This reduced time step is needed to avoid numerical instabilities which can occur when large amounts of vapour diffuse quickly at high obliquity, and is the same value used by Zent et al. (1993).

In the regolith model, the concentration of water in a volume of regolith, σ, is decomposed into three states: vapour contained within the pore spaces (ϕn), vapour adsorbed onto regolith grains (α) and pore ice (ζ), all measured in kg m^{-3}. Thus,

$$\sigma = \phi n + \alpha + \zeta, \tag{1}$$

where ϕ is the porosity of the regolith and n is the vapour density. The model uses the adsorption isotherm of Fanale and Cannon (1971), which has been used extensively in previous studies of regolith diffusion (e.g. Zent et al., 1993; Mellon and Jakosky, 1993, 1995; Mellon et al., 1997; Böttger et al., 2005). Unlike the scheme of Böttger et al. (2004, 2005) which used the σ value in the diffusion calculation, we use the $\sigma - \zeta$ value. This removes the assumption from the original scheme that all the ice in a grid box turns to vapour and adsorbed water before diffusion is calculated. (See Appendix A for a description of the diffusion model.)

Böttger et al. (2004, 2005) used a constant diffusion coefficient specified in advance, but here we allow the diffusion coefficient to vary in time and space, and consider both Fickian and Knudsen diffusion. In this case, the effective diffusion coefficient, D, is given by the Bosanquet relation, $D^{-1} = D_{\rm F}^{-1} + D_{\rm K}^{-1}$ (where $D_{\rm F}$ and $D_{\rm K}$ are the Fickian and Knudsen diffusion coefficients respectively). For Fickian diffusion in a porous medium, the diffusion coefficient is that given by Mason and Malinauskas (1983):

$$D_{\rm F} = \frac{\phi}{\tau} D_{12}, \tag{2}$$

where D_{12} is the mutual diffusion coefficient, τ is the tortuosity (which characterizes the convoluted nature of the porous pathways) and the ratio ϕ/τ is the 'obstruction factor'. The porosity is parameterized as in Mellon and Jakosky (1993), giving

$$\phi = \phi_0(1 - \zeta/\rho_{\rm ice}\phi_0), \tag{3}$$

where ϕ_0 is the ice-free porosity. We take $\phi_0 = 0.4$, which falls within the range determined at the Viking Lander 1 site (Moore and Jakosky, 1989;

Boynton et al., 2002). The tortuosity is parameterized as in Hudson (2008), giving

$$\tau \approx \tau_0 (1 - \zeta/\rho_{\rm ice}\phi_0)^{-1}, \tag{4}$$

where τ_0 is the ice-free tortuosity, parameterized as $\tau_0 = \phi_0^{-1/3}$ (Millington, 1959). This parameterization produces results in agreement with both simulations (Zalc et al., 2004) and measurements using Mars-analogue soils (Sizemore and Mellon, 2008). Combining Equations 3 and 4, the obstruction factor becomes

$$\frac{\phi}{\tau} = \phi_0^{4/3} \left(1 - \frac{\zeta}{\rho_{\rm ice}\phi_0}\right)^2. \tag{5}$$

The coefficient of mutual diffusion for the case of water vapour diffusing into CO_2 is that of Wallace and Sagan (1979):

$$D_{12} = D_{\rm H_2O,CO_2} = 0.1654\,{\rm cm^2\,s^{-1}}\,\frac{p_{\rm ref}}{p(z)}\left[\frac{T(z)}{T_{\rm ref}}\right]^{3/2}, \tag{6}$$

where $T(z)$ and $p(z)$ are the temperatures and pressures at a distance z below the surface, and $T_{\rm ref} = 273.15\,{\rm K}$ and $p_{\rm ref} = 1013\,{\rm hPa}$ are reference temperatures and pressures. Since the regolith model only extends down to $\sim$20 m the pressure change is negligible, so we take $p(z) = p_{\rm surf}$. Finally, combining Equations 2, 5 and 6 gives

$$D_{\rm F} = 0.1654\,{\rm cm^2\,s^{-1}}\,\phi_0^{4/3}\frac{p_{\rm ref}}{p_{\rm surf}}\left(1 - \frac{\zeta}{\rho_{\rm ice}\phi_0}\right)^2\left[\frac{T(z)}{T_{\rm ref}}\right]^{3/2}. \tag{7}$$

The Knudsen diffusion coefficient is proportional to the mean velocity of the diffusing molecules. We use the parameterization given by Evans et al. (1961):

$$D_{\rm K} = \frac{\pi}{8+\pi}\frac{\phi}{1-\phi}\frac{\bar{\nu}\bar{r}}{\tau}, \tag{8}$$

where $\bar{r}$ is the average pore size in the regolith and $\bar{\nu}$ is the mean velocity of the diffusing molecules, given by $\bar{\nu} = (8k_{\rm B}T/\pi m_{\rm w})^{1/2}$, with $k_{\rm B}$ the Boltzmann constant and $m_{\rm w}$ the molecular mass of water.

The value of $\bar{r}$ will vary with location. Soil properties have been studied at the locations of the Viking landers, Pathfinder, Spirit, Opportunity, Phoenix and Curiosity. A recent overview of soil properties is given by Demidov et al. (2015). The spatial variation of soil properties is difficult to account for in a GCM. Flasar and Goody (1976) used a value of $\bar{r} = 1\,\mu$m for their

calculations of Knudsen diffusion, while Fanale et al. (1986), Mellon and Jakosky (1993) and Mellon et al. (1997) use a value of 10 μm. In studying the pore sizes in JSC Mars-1 simulant, Sizemore and Mellon (2008) found that grains in the 38–63 μm and 250–500 μm size ranges had peaks in their pore-size distribution at around 10 μm and 100 μm respectively. Using a value of between 10–100 μm in our scheme results in a diffusion coefficient during the daytime of 4–7 $\mathrm{cm^2\,s^{-1}}$, which is in agreement with previous studies of the diffusion coefficient (e.g. Chevrier et al., 2007; Sizemore and Mellon, 2008; Hudson et al., 2007; Hudson and Aharonson, 2008; Hudson et al., 2009). A smaller value, e.g. 1 μm, would result in a diffusion coefficient $\sim$0.7 $\mathrm{cm^2\,s^{-1}}$, which is comparable to the value found for heavily salt-encrusted soils, but not the general regolith (Hudson and Aharonson, 2008). Since the majority of landers determined grain sizes $\lesssim 100\,\mu$m, we use a pore size of $\bar{r} = 10\,\mu$m, in line with the results of Sizemore and Mellon (2008).

From Equations 7 and 8 it can be seen that the diffusion coefficient gets larger as temperature increases and pressure decreases. For example, in the Hellas basin at night we have $D \approx 1.7\,\mathrm{cm^2\,s^{-1}}$, while on the Tharsis Plateau and on top of Olympus Mons during the daytime the diffusion coefficients are around $5\,\mathrm{cm^2\,s^{-1}}$ and $6\,\mathrm{cm^2\,s^{-1}}$ respectively. (The scheme of Böttger et al. (2005) used a constant diffusion coefficient of $1\,\mathrm{cm^2\,s^{-1}}$, so diffusion operates more quickly in our simulations.) Thus, the flux of water into or out of the regolith will be affected by the altitude of the surface and the temperature, along with the amount of water in the near-surface layer. This flux is determined via a balance of the fluxes at the regolith–atmosphere boundary. For the regolith, the flux is $F_{\mathrm{reg}} = \kappa_{\mathrm{reg}}(n_1 - n_{\mathrm{b}})$, while for the atmosphere the flux is $F_{\mathrm{atm}} = \rho\kappa_{\mathrm{atm}}(q_1 - q_{\mathrm{b}})$, and we require $F_{\mathrm{atm}} = -F_{\mathrm{reg}}$. (Here the subscript '1' represents the first regolith or atmosphere layer, the subscript 'b' represents the regolith–atmosphere boundary, q is the water vapour mass mixing ratio in the atmosphere, and ρ is the atmospheric density at the surface.) The coefficients in the flux terms for the regolith and atmosphere are given by $\kappa_{\mathrm{reg}} = D/z_{0.5}$ and $\kappa_{\mathrm{atm}} = C_{\mathrm{d}}|\mathbf{u}|$, with $z_{0.5}$ the depth to the first regolith layer midpoint, C_{d} the drag coefficient and $|\mathbf{u}|$ the magnitude of the near-surface wind. The presence of surface CO_2 ice or water ice shuts off the regolith-atmosphere interaction, though vertical redistribution of water already in the regolith can still occur through diffusion and phase changes (lateral transport is not modelled).

The presence of subsurface ice affects the regolith thermal inertia, which in turn affects the regolith temperature. While models of thermal conductiv-

ity have suggested that even small amounts of pore ice can rapidly increase the thermal conductivity of the regolith (e.g. Mellon et al., 1997; Piqueux and Christensen, 2009), recent laboratory experiments have shown that the thermal conductivity of an ice-regolith mix increases approximately linearly with ice content (Siegler et al., 2012). As such, when ice is present in the subsurface we model the thermal conductivity, k, following Equation 36 of Siegler et al. (2012):

$$k(f,T) = 0.8\phi_0 f k_{\mathrm{ice}}(T) + k_{\mathrm{dry}}, \tag{9}$$

where k_{dry} is the thermal conductivity of the ice-free regolith (horizontally varying but constant with depth) which is derived from TES thermal inertia data (Mellon et al., 2000), $f = \zeta/\rho_{\mathrm{ice}}\phi_0$ is the filling fraction, and $k_{\mathrm{ice}}(T) = 488.19/T + 0.4685$ is the thermal conductivity of ice at temperature T (Hobbs, 1974). As an example, taking a dry regolith conductivity of $k_{\mathrm{dry}} = 0.04\,\mathrm{W\,m^{-1}\,K^{-1}}$ (corresponding to a thermal inertia of around 250 tiu) and taking all the pore space to be filled with ice, the thermal conductivity for the ice-rich layer varies from $0.77\,\mathrm{W\,m^{-1}\,K^{-1}}$ (at 270 K) to $1.23\,\mathrm{W\,m^{-1}\,K^{-1}}$ (at 150 K). This is lower than the values of 2.5–2.8 $\mathrm{W\,m^{-1}\,K^{-1}}$ used in previous studies (Mellon et al., 1997, 2004; Chamberlain and Boynton, 2007; Zent, 2008; Williams et al., 2015), but comparable to values used by Schorghofer and Aharonson (2005) and Schorghofer (2007).

3. Simulations performed

Calculations show that the obliquity of Mars over the last 5 million years has varied between around 15°–35°, while beyond this time (up to 20 million years ago) the obliquity varied between around 25°–45° (Laskar et al., 2004, and see also Figure 1). Each obliquity cycle lasts roughly 10^5 yr and, combined with changes to eccentricity and precession (varying on time-scales of around 10^5 yr and 50 kyr respectively), a variety of different orbital configurations are possible. GCM simulations cannot be performed over an entire obliquity cycle due to the computation time required. Thus, in order to study the effects of various orbital parameters and dust conditions on the distribution of subsurface water (in particular the locations of stable subsurface ice deposits), 24 simulations were performed. These simulations are essentially 'snapshots' at various points throughout Mars' history. The parameters varied were the obliquity ($\varepsilon = 15°$, 30° and 45°), eccentricity ($e = 0$

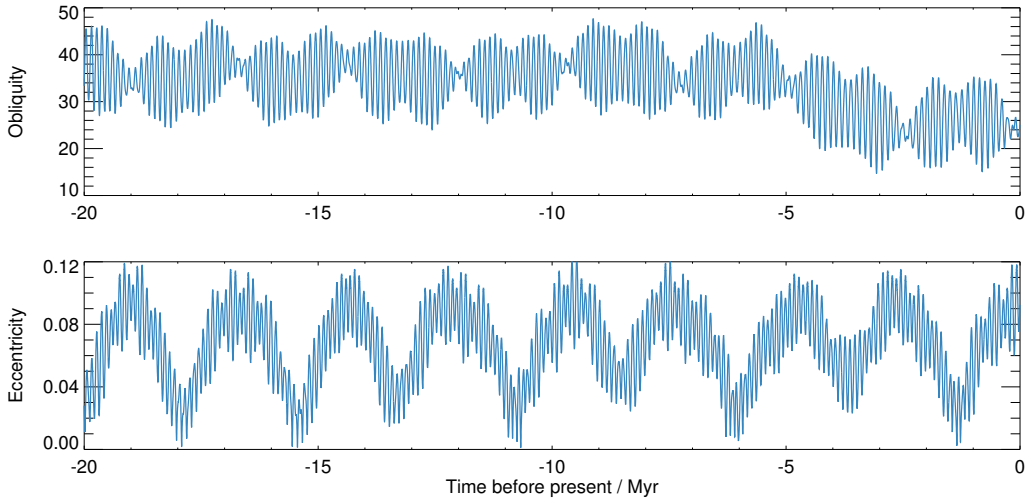

Figure 1: Variation of obliquity and eccentricity over the past 20 million years. Solar longitude of perihelion varies much more regularly, and is not shown. Data are from Laskar et al. (2004).

and 0.1), solar longitude of perihelion ($L_\mathrm{p} = 90°$ and 270°) and visible dust optical depth ($\tau_\mathrm{vis} = 0.3$ and 3). For validation purposes, a simulation was also performed for present-day conditions.

Table 1 displays each of the simulations performed and the combination of parameters used, while Figure 2 shows the obliquities and surface ice reservoirs used. Simulations 1–18 have surface ice reservoirs defined at the poles, as they represent Mars as it moves from low obliquity to higher obliquity, and at low obliquity ice forms in the polar regions (e.g. Levrard et al., 2004). Ice caps are placed at both poles for the lowest obliquity, while at other obliquities the ice caps are placed over the pole experiencing summer during aphelion (the ice caps extend from the poles to ±67.5° latitude, i.e. all of the first or last rows of the model grid). Simulations 19–24 represent Mars having been at its highest obliquity, and beginning to move towards lower obliquity. We assume that the polar ice caps have sublimed away completely, and a tropical ice source is defined over the Tharsis region, as in previous modelling work (e.g. Jakosky and Carr, 1985; Levrard et al., 2004; Forget et al., 2006; Madeleine et al., 2009). While the models are initialised with pre-defined infinite reservoirs of ice, surface ice can, and indeed does, form elsewhere due to the transport of water and the sedimentation of ice particles.

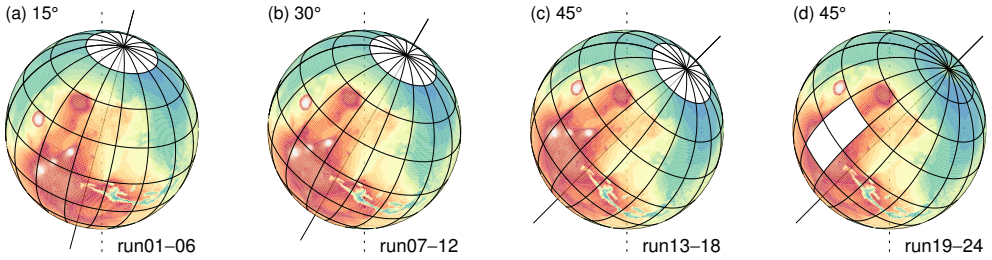

Figure 2: Overview of the obliquities and surface ice reservoirs (white shading) for the simulations performed. The grid spacing corresponds to T5 resolution. In (a) there is also a south polar ice cap. In (b) and (c) the ice cap can either be at the north or south pole, but not both. In (d) there is an ice reservoir in the Tharsis region, but no permanent polar ice caps are specified. Coloured shading denotes surface topography at 1° resolution.

This ice can then sublime if temperatures are high enough. The atmospheric mass and solar luminosity are kept unchanged, as these simulations model the relatively recent past.

For each simulation, initial regolith temperatures were obtained from 'spin up' runs with no water cycle, performed for 100 Mars years. The regolith was initialised at each grid point with $2\,\mathrm{kg\,m^{-3}}$ of water, existing primarily as adsorbed water, which is the same value used by Zent et al. (1993) and Böttger et al. (2005). This is because if the regolith is completely dry, any vapour sublimed from the surface ice reservoirs preferentially diffuses into the nearby surrounding regolith, resulting in an excessively dry water cycle at lower obliquities. (It is worth noting that because of the increased vapour abundances at high obliquity, simulations initialised with either a completely dry regolith, or with $2\,\mathrm{kg\,m^{-3}}$ of water, produce the same results after a few hundred Mars years.) The value of $2\,\mathrm{kg\,m^{-3}}$ is not large enough to form any subsurface ice without further diffusion of water from the atmosphere.

When discussing the geographic distribution of water, we will generally refer to three regions: the tropics (±22.5° latitude), the mid-latitudes (22.5°–67.5° in each hemisphere) and the polar regions (67.5°–90° in each hemisphere). When discussing the number of years simulations have been run for we are referring to Mars years, but note that the time periods of 5 Myr and 5–20 Mya correspond to Earth years. For brevity, we will hereafter refer to 'water ice' and 'water vapour' as simply 'ice' and 'vapour'.

Name	ε	L_p	e	τ_vis	Ice reservoir
run01	15	90	0.1	0.3	Both poles
run02	15	90	0.1	3	Both poles
run03	15	270	0.1	0.3	Both poles
run04	15	270	0.1	3	Both poles
run05	15	-	0	0.3	Both poles
run06	15	-	0	3	Both poles
run07	30	90	0.1	0.3	South pole
run08	30	90	0.1	3	South pole
run09	30	270	0.1	0.3	North pole
run10	30	270	0.1	3	North pole
run11	30	-	0	0.3	North pole
run12	30	-	0	3	North pole
run13	45	90	0.1	0.3	South pole
run14	45	90	0.1	3	South pole
run15	45	270	0.1	0.3	North pole
run16	45	270	0.1	3	North pole
run17	45	-	0	0.3	North pole
run18	45	-	0	3	North pole
run19	45	90	0.1	0.3	Tropics
run20	45	90	0.1	3	Tropics
run21	45	270	0.1	0.3	Tropics
run22	45	270	0.1	3	Tropics
run23	45	-	0	0.3	Tropics
run24	45	-	0	3	Tropics

Table 1: Overview of the parameters used for each simulation: obliquity (ε), solar longitude of perihelion (L_p), eccentricity (e) and visible dust optical depth (τ_vis). When the eccentricity is zero, the value of L_p is no longer relevant. Simulations 1–18 represent Mars moving from low to higher obliquity, while simulations 19–24 represent Mars moving from high to lower obliquity.

4. Model validation

Before performing simulations for past climates, the model was validated for the present-day atmosphere (with $\varepsilon = 25.19°$, $L_\mathrm{p} = 251°$, $e = 0.093$, and initially $2\,\mathrm{kg\,m^{-3}}$ of water at each gridpoint in the regolith). The dust distribution used in the model is obtained from the dust maps of Montabone et al. (2015). Figure 3a shows the vapour column distribution resulting from the assimilation of TES temperature profiles and vapour columns at T31 resolution (see Steele et al., 2014b). The first half of the period shown ($L_\mathrm{S} = 180°$–$360°$) corresponds to Mars year 24, with the second half corresponding to Mars year 25. Figure 3(b–d) shows the results of a T5 simulation after 800 years.

Comparing the vapour columns, it can be seen that the main features of the water cycle are captured by the T5 simulation, with vapour peaks in the polar regions during summertime, dry polar regions and mid-latitudes in winter, and a relatively dry region between 0°–30°S around southern hemisphere summer. The time of peak vapour abundance in the southern hemisphere occurs later in the T5 simulation than in the assimilation. This is due to increased dust cover in the south polar region of the T5 simulation (caused by smoothing of the dust maps to T5 resolution). There were no observations to assimilate for a period around $L_\mathrm{S} = 15°$, resulting in the water cycle in the assimilation being slightly dry around this time. In general the differences in the vapour columns between the assimilation and T5 simulation are within the $5\,\mathrm{pr}\text{-}\mu\mathrm{m}$ uncertainty of the TES data (Smith, 2004). In terms of ice clouds (Figure 3c), the model captures the aphelion cloud belt, the north polar hood (which extends to the poles) and the south polar hood (which forms an annulus around the south pole). These are in good agreement with observations (e.g. Smith, 2004; Benson et al., 2010, 2011).

The subsurface water content is shown in Figure 3d. Comparing with MONS observations (e.g. Feldman et al., 2004; Maurice et al., 2011), the model agrees in terms of the spatial distribution of subsurface water, with a dry area circling the globe in the southern mid-latitudes, and relatively large subsurface water contents around the Tharsis, Arabia Terra and south polar regions. (The north polar region is dry, as we defined this to be the location of a permanent ice cap, so no diffusion into the regolith occurred.) While the spatial distribution shows broad agreement, the subsurface water abundances at high latitudes have not reached the values observed by MONS, as diffusion is a slow process and the simulation time of 800 years is relatively short.

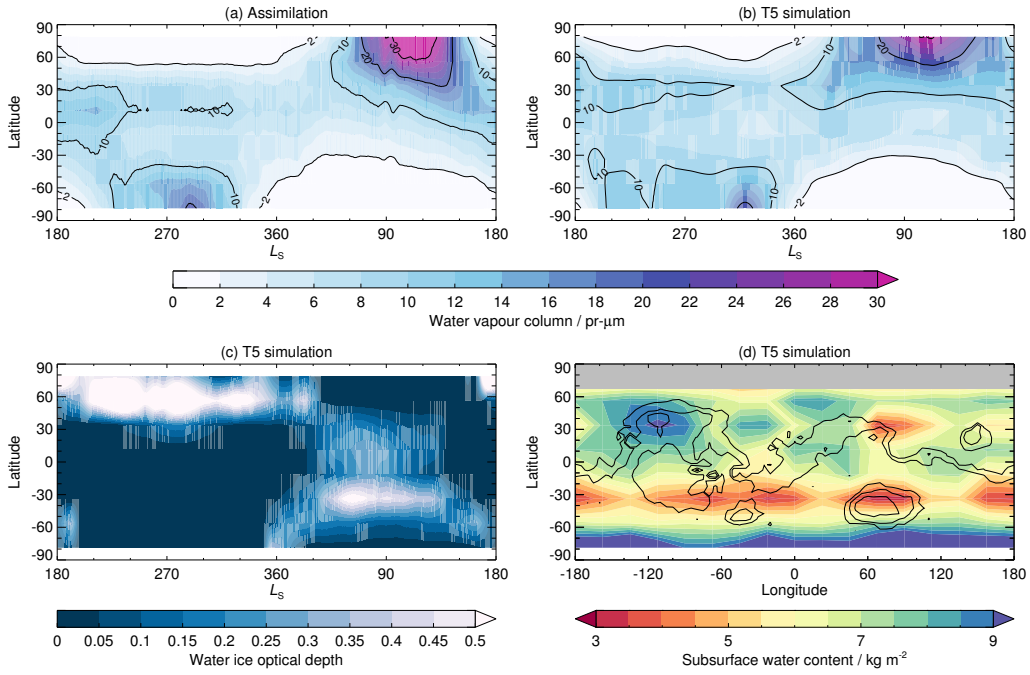

Figure 3: Validating the water cycle at T5 resolution for present-day conditions. Panels (a–c) show zonal averages as a function of latitude and time, and are (a) the vapour column distribution from a T31 assimilation (Steele et al., 2014b), (b) the vapour column distribution from a T5 simulation, and (c) the ice optical depth from a T5 simulation. Panel (d) shows the subsurface water content (adsorbed water, ice and vapour) between 5 cm–2 m below the surface after 800 years of simulation. In panel (d) the black contours show topography and the grey shading shows the location of the polar ice cap.

A one-dimensional simulation was also performed at the location of the Phoenix lander (68.2°N, 125.7°W) in order to validate the diffusion model used in the GCM. The required inputs (surface and subsurface temperatures, surface pressure and near-surface vapour) were taken every 30 minutes from the GCM simulation of the present-day atmosphere. Near-surface vapour amounts are negligible for the majority of the year due to cold temperatures. Interaction between the atmosphere and regolith only occurs between L_S = 68°–126° when surface ice deposits sublime. During this time, the average near-surface vapour mass mixing ratio is $\sim 2 \times 10^{-4}$, with a peak value of $\sim 5 \times 10^{-4}$. The regolith was initially dry, and the simulation was performed for 1000 years.

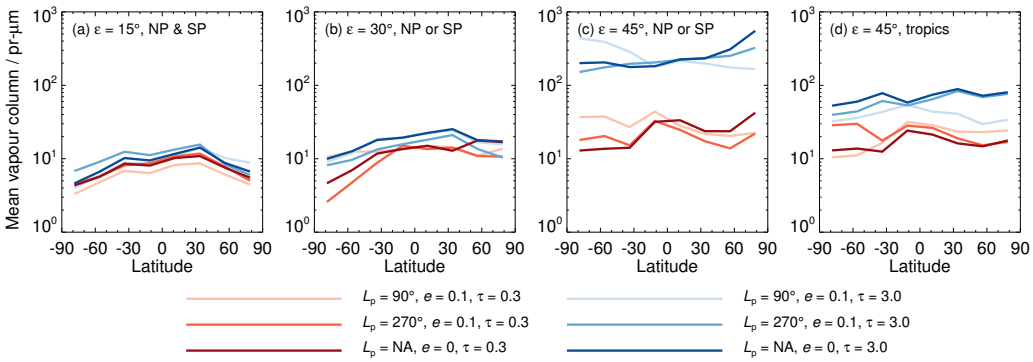

Figure 4: Zonally- and temporally-averaged water vapour columns from year 800 of each of the 24 simulations performed. The obliquities and ice cap locations are labelled in each plot; see Table 1 for full details.

The results show subsurface ice to be stable at a depth of ∼9.5 cm, with pore ice temporarily forming in a layer a few centimetres deep on top of the ice layer between $L_S = 75°$–$90°$ The depth of 9.5 cm is comparable to the deepest depth to ice observed by Phoenix, but deeper than the mean depth of 4.6 cm (Mellon et al., 2009). However, considering the variability in ice table depths observed over a relatively small location (with one trench excavated to 18.3 cm showing no ice), and the variations in thermal inertia and slope angle which we do not take into account here but which can affect ice stability (Aharonson and Schorghofer, 2006), our model results are comparable to the observations. The adsorbed water values above the ice table in our model are ∼2–8 kg m^{-3}, which corresponds to ∼0.1–0.5% by mass. These are in line with adsorbed water amounts measured on martian regolith analogs (Pommerol et al., 2009), and are consistent with regolith observations by Phoenix, where it was inferred that adsorbed water was responsible for variabilities in the nature and cohesive strength of the soils (Arvidson et al., 2009).

5. Regolith-atmosphere interaction over the last 5 Myr

5.1. 15° obliquity

Considering first the $\varepsilon = 15°$ simulations (with ice caps in both polar regions), there is little difference in the water cycle when changing the eccentricity or solar longitude of perihelion (see Figure 4a). Changing the dust distribution does have an effect, however, with the atmosphere in the

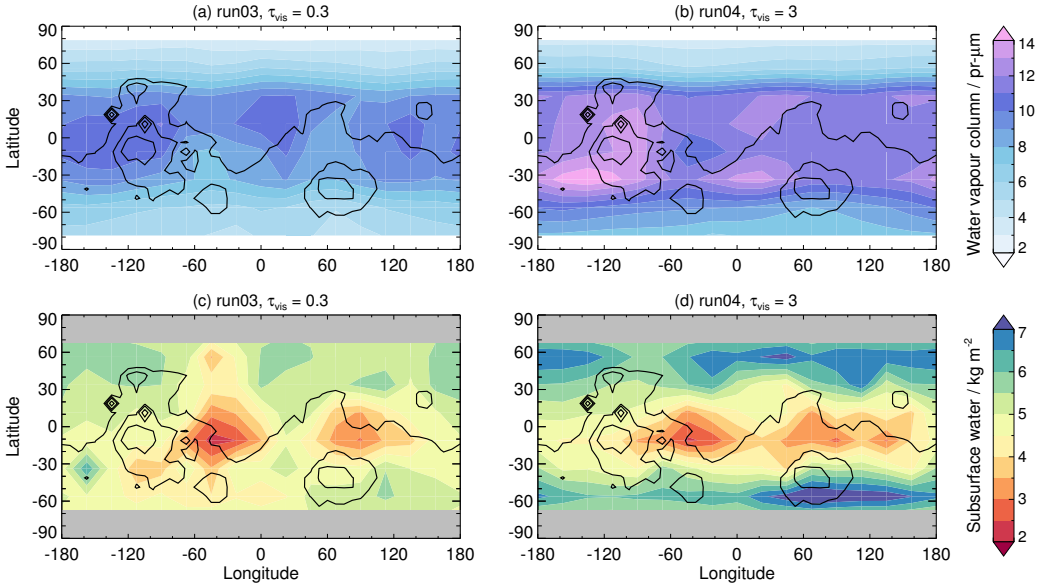

Figure 5: Atmospheric and subsurface water contents from two simulations at $\varepsilon = 15°$ with different atmospheric dust contents. (a–b) The mean annual vapour column distribution, scaled to a reference pressure of 610 Pa to remove the effects of topography. (c–d) The subsurface water content (adsorbed water, ice and vapour) between 5 cm–2 m below the surface after 800 years of simulation. Black contours show topography, and grey shading in the lower panels shows the locations of the polar ice caps.

dusty simulations being around 2–4 pr-μm wetter than the clear simulations. This can be seen in Figure 5(a,b), which shows the mean annual vapour column distribution from run03 and run04 (the other simulations show similar trends). The dustier simulations are wetter due to warmer atmospheric temperatures. In the tropics, daytime temperatures in the dusty simulations are 10–20 K warmer than in the clear simulations at altitudes below 5 km, and 30–40 K warmer at altitudes above 15 km. In the polar regions during summer, the temperatures below 15 km are 5–10 K warmer in the dusty simulations, and above 25 km they are 30–40 K warmer. These warmer temperatures strengthen the meridional circulation, allowing more vapour to be transported away from the subliming polar ice caps in the summer.

The increased transport from the polar ice caps, combined with cooler surface temperatures in the dusty simulations, results in the regolith at the edges of the ice caps having a larger water abundance than in the clear

simulations. This can be seen in Figure 5(c,d), which shows the subsurface water content (in the adsorbed and vapour phases, as no ice has formed) between 5 cm–2 m. After 800 years of simulation, the water content in these relatively wet regions of the subsurface is only increasing slowly (by around 0.1–1 $\mathrm{g\,m^{-2}\,yr^{-1}}$). Considering that the mean annual temperature of the subsurface in these regions is ∼180 K, it would take many thousands of years for the amount of water adsorbed to be in equilibrium with the atmosphere. In the tropics there are two dry areas in regions with relatively high thermal inertia.

5.2. 30° obliquity

At $\varepsilon = 30°$, sublimation from the polar ice caps is increased compared to at $\varepsilon = 15°$, hence the water cycle is globally wetter. Peak vapour columns are ∼100 pr-μm, compared to ∼15 pr-μm at $\varepsilon = 15°$, and mean vapour columns are around 1.5–2 times as large as at $\varepsilon = 15°$ (see Figure 4b). In terms of the spatial distribution of subsurface water, Figure 6 shows the global subsurface water content between 5 cm–2 m below the surface. To enable a better spatial resolution, the results of the T5 simulation at year 800 were used to initialise a T31 simulation which ran for an additional 20 years. The stability of subsurface ice reacts very quickly to changing temperatures, so 20 years of simulation is long enough to gain meaningful results from the higher resolution simulations. (Stable subsurface ice is defined as ice which does not lose mass over the course of the 20-year simulation.) Figure 6 ignores the dry upper ∼5 cm where little water exists due to the warm temperatures limiting the amount of vapour adsorbed on to the regolith grains. The water content is calculated to a depth of 2 m as this is the depth to which vapour had diffused at the end of the simulation.

It is clear that there are certain locations where subsurface water preferentially accumulates. The polar regions contain the most water, with up to 20 $\mathrm{kg\,m^{-2}}$ existing in both the adsorbed and ice phases after 800 years of simulation. Away from the polar regions there are locally large water abundances in the Arabia Terra region (centred at around 20°E near the equator), south-east of Elysium Mons (on the dichotomy boundary between Elysium Planitia and Terra Cimmeria) and around Alba Mons, though no stable subsurface ice is present. In the northern hemisphere, three relatively dry areas are observed: two surround the relatively wet Arabia Terra region, with a third to the north-east of Elysium Mons. In the southern mid-latitudes the

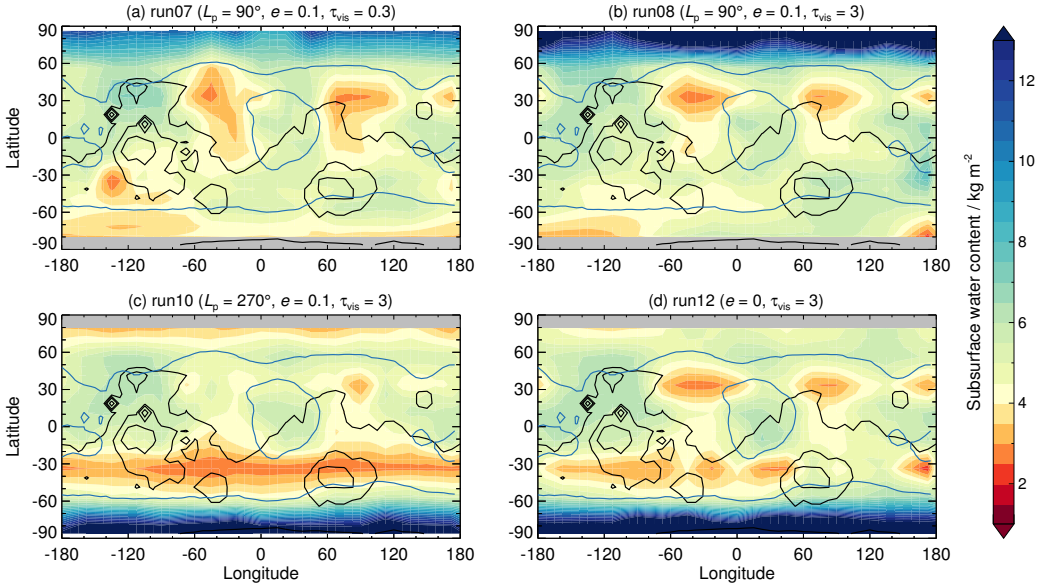

Figure 6: Total subsurface water content (adsorbed water, ice and vapour) between 5 cm–2 m below the surface after 820 years of simulation (800 years at T5 resolution and 20 years at T31 resolution). Black contours show topography, while blue contours highlight areas of increased subsurface water (at each pole and in two regions in the tropics) observed by MONS (Feldman et al., 2004). Polar ice cap locations are shown with grey shading.

water distribution is dependent upon the location of the ice cap. For a south-polar ice cap as in Figure 6(a,b) the southern mid-latitudes do not have any particularly dry areas, while for a north-polar ice cap as in Figure 6(c,d) this region is relatively dry. The subsurface water distribution away from the polar regions is little affected by changes to the solar longitude of perihelion, the eccentricity or the dust content of the atmosphere, even though these lead to differences in the distribution and peak values of vapour. Instead, the distribution is largely determined by the regolith properties, with regions of relatively little water corresponding to regions of high thermal inertia and low albedo.

Comparing with MONS observations (Feldman et al., 2004; Maurice et al., 2011), the simulated and observed subsurface water distributions show good spatial agreement, with the simulations with a north-polar ice cap (Figure 6c,d) displaying the best agreement. The similarity is because while the water cycle at $\varepsilon = 30°$ is wetter than in the present day, the regolith

temperatures in the tropics and mid-latitudes are broadly the same, and there still isn't enough near-surface vapour to form ice from diffusion. Thus, the simulation results suggest that the subsurface water distribution revealed by MONS is likely to occur for a range of obliquities close to that of today, when the atmospheric water content is supplied by a north polar ice cap.

The MONS observations of the polar regions (e.g. Feldman et al., 2007; Maurice et al., 2011) show increased subsurface water abundances and decreased burial depths centred roughly at 135°W, 70°N and 90°E, 70°S. From the GCM results, these areas correspond to regions of increased atmospheric water content due to transport by topographically-steered flows to the west of Tharsis during northern hemisphere summer, and stationary waves to the east of Hellas during southern hemisphere summer (Forget et al., 2006; Steele et al., 2014b). During autumn, the cooling surface temperatures and locally large vapour amounts mean the flux of vapour into the regolith is greater in these regions compared to elsewhere. For example, at 90°E in run12, the flux of vapour into the regolith is greater at 70°S ($\sim$6 g m^{-2} sol^{-1}) than it is at 60°S or 80°S ($\sim$3 g m^{-2} sol^{-1}). Similar values occur in run08 at 135°W and 60–80°N. As these regions of increased subsurface water are the result of vapour transport due to topographic features, it is likely they will also experience increased subsurface water at different obliquities. (Feldman et al. (2005) have previously linked regions of decreased subsurface water to the east and west of Arabia in the present day with the location of western boundary currents.)

While the spatial distribution of subsurface water agrees well after 820 years of simulation, the water abundances have not yet reached the values observed by MONS. For example, the wet region in Arabia Terra is $\sim$0.8% water by mass (compared to $\sim$8% in the observations), while the polar regions are around 2% (compared to values up to $\sim$50% in the observations). However, the wet regions in the tropics are still slowly gaining water by around 20–40 g m^{-2} yr^{-1} (in the form of adsorbed water), and subsurface ice is increasing at the polar regions (but the small areal extent means it has little impact on the global mass calculation). However, even if the wet regions in the tropical subsurface were in equilibrium with the atmosphere, then the subsurface water abundance in the upper 2 m of regolith would not reach the 10% value observed by MONS (which would require $\sim$170 kg m^{-3} of subsurface water). It has been proposed that hydrous minerals may be responsible for some of the observed hydrogen near the equator (e.g. Bish et al., 2003; Wang et al., 2013; Karunatillake et al., 2014).

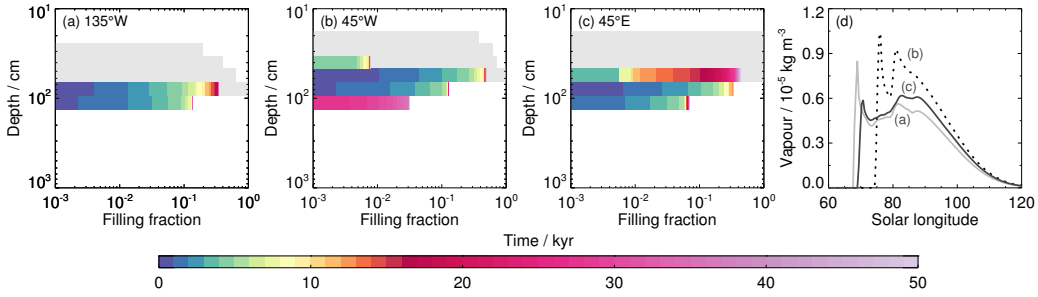

Figure 7: (a–c) Variation of the filling fraction ($f = \zeta/\rho_{\rm ice}\phi_0$) with depth and time for three different longitudes at 78°N. Coloured shading shows the ice evolution over 50 kyr. Grey shading shows the result after initialising the regolith with ice abundances of $f = 0.5$ from the surface down to the layer with the largest ice abundance after 50 kyr. (d) Variation of the near surface water vapour abundance over part of the year at the three locations in panels (a–c).

To investigate the build-up of ice over the polar regions further, a series of one-dimensional simulations were performed with latitudes of ±78° and longitudes of ±45°E and ±135°E. The simulations were run for 50 kyr, with the relevant data (surface and subsurface temperatures, surface pressure and near-surface vapour) taken every 30 minutes from year 820 of run07–run12. (After 820 years these values in the global model have reached equilibrium, and repeat each year.) The results for three locations from run08 are shown in Figure 7(a–c), with the corresponding near-surface water vapour abundances shown in panel (d). The results from the other simulations are similar, so are not shown.

Subsurface ice begins to form when vapour abundances reach the saturation value. Due to the initially low vapour abundance in the regolith, this generally corresponds to the depth where the coldest temperatures are found, though in reality will be dependent on the nature of the pore spaces (e.g. Hudson et al., 2009). Over time the ice builds up and the regolith porosity is reduced, which limits the transport of vapour deeper into the regolith below the ice layer. For example, for a filling fraction of $f = 0.5$, the Fickian diffusion coefficient is 25% of the ice-free value. The vapour values above the ice layer then increase, eventually reaching saturation and allowing ice to form. Thus, the ice table migrates upwards over time. After 50 kyr, the top of the ice layer has reached depths of ∼30–70 cm (depending on location), with the ice extending to depths just below 1 m. To see to what depth ice

would be stable at these three locations given more time, we took the results after 50 kyr and filled the regolith with ice from the surface down to the layer with the largest ice abundance. We then ran the simulations until the ice distributions reached equilibrium. (Ice in the upper few centimetres of the regolith is unstable and rapidly sublimes.) The results are shown by the grey shading in Figure 7(a–c). As can be seen, ice is stable at depths of ∼20 cm, which is similar to the MONS observations (e.g. Maurice et al., 2011).

5.3. Equilibrium ice table depth

The previous two sections have looked at the subsurface water distributions resulting from the explicit calculation of vapour diffusion in the regolith. However, it is also possible to determine the depth at which buried ice is in equilibrium with the atmosphere from the regolith temperatures and near-surface vapour values. We take this depth to be the point in the regolith at which the mean annual saturated vapour pressure, $\bar{e}_{\rm sat}$, is equal to the mean annual atmospheric vapour pressure in the near-surface layer, $\bar{e}_{\rm vap}$. This same procedure has been used in other studies, such as Mellon and Jakosky (1995); Mellon et al. (2004); Schorghofer and Aharonson (2005); Chamberlain and Boynton (2007). We perform equilibrium depth calculations at T31 resolution using the orbital parameters and dust optical depths appropriate for the simulations at $\varepsilon = 15^\circ$ and $\varepsilon = 30^\circ$ (see Table 1). The $\bar{e}_{\rm vap}$ values are obtained from year 820 of the relevant simulations (after 800 years at T5 resolution and 20 years at T31 resolution).

The regolith thermal inertias initially correspond to ice-free values, except in the lowest model layer where they are amended to those of an ice-regolith mix using Equation 9 (with $f = 1$, taking all the pore space to be filled with ice). The model was then run for a year, and the regolith temperatures were used to find $\bar{e}_{\rm sat}$ in the model layer above the ice-regolith mix. If $\bar{e}_{\rm sat} < \bar{e}_{\rm vap}$, then the thermal inertia of this layer was also amended to that of an ice-regolith mix. The model was then run for another year with this new thermal inertia distribution, and the procedure was iterated (increasing the thermal inertia of the layer above) until $\bar{e}_{\rm sat} = \bar{e}_{\rm vap}$.

The result of one $\varepsilon = 15^\circ$ simulation is shown in Figure 8a. The other simulations at this obliquity follow similar trends in the polar regions, but there are differences in the tropics and mid-latitudes. Figure 8b shows the result for the present-day. At $\varepsilon = 15^\circ$ it can be seen that polewards of ∼60° in both hemispheres, ice can be stable at shallow depths below the surface. In the region around Olympus Mons and Alba Mons, ice can be stable at

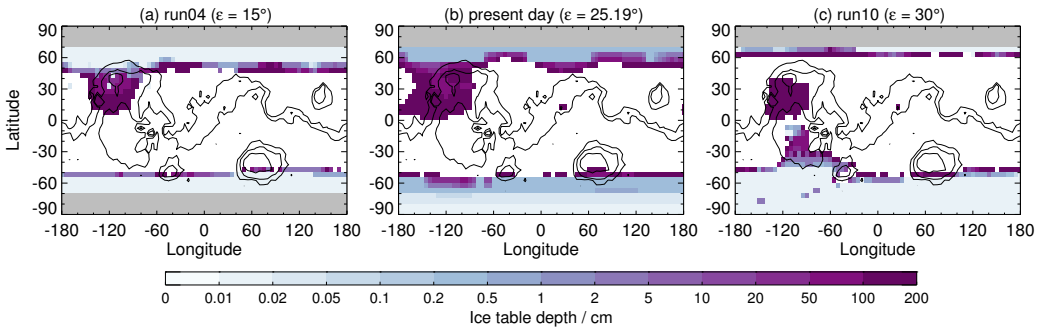

Figure 8: Maps of the ice table stability depth for simulations at (a) $\varepsilon = 15°$, (b) $\varepsilon = 25.19°$ and (c) $\varepsilon = 30°$. The $\varepsilon = 25.19°$ simulation uses present-day orbital parameters and dust maps. The $\varepsilon = 15°$ and 30° simulations have $L_\mathrm{p} = 270°$, $\tau_\mathrm{vis} = 3$ and $e = 0.1$. The surface ice reservoirs are shown with grey shading. White shading indicates regions where no stability occurred down to a cut-off depth of 2 m. (We use this cut-off depth as below ∼2 m the regolith temperatures are not affected by the seasonally varying surface temperatures, and remain as initialised.) Black contours show topography.

depths of ∼0.5–2 m in the dusty simulations, but this region of stability is not present in the clear simulations, or the simulations with zero eccentricity (as vapour values are lower and/or surface temperatures are warmer). In the present-day simulation, the ice table in the polar regions is slightly deeper than at $\varepsilon = 15°$ due to the warmer mean annual temperatures. The region of ice stability around Olympus Mons and Alba Mons is larger than at $\varepsilon = 15°$, as more vapour is sublimed from the polar ice cap and hence mean annual near-surface vapour amounts are larger.

Similar calculations at low obliquity were performed by Mellon and Jakosky (1995) and Chamberlain and Boynton (2007), although using one-dimensional models. At low obliquity, they determined that ice would not be stable anywhere between ±60° latitude, while our results show ice can be stable in the region around Olympus Mons and Alba Mons. The reason for this difference is likely due to the fact that in our $\varepsilon = 15°$ simulations the vapour columns in this region can reach ∼15 pr-μm, while Mellon and Jakosky (1995) assumed a vapour column of 2.62 pr-μm for $\varepsilon = 19.55°$, and Chamberlain and Boynton (2007) assumed a value of 0.33 pr-μm for $\varepsilon = 15°$. Thus, our simulations have larger near-surface vapour values, meaning ice stability can occur in locations with higher regolith temperatures.

The same procedure can be carried out for the $\varepsilon = 30°$ simulations. The

result of one simulation is shown in Figure 8c. Again, the other simulations follow similar trends in the polar regions, with differences around the Tharsis region. Compared to the previous results, there is a slight reduction in the areal extent of stable subsurface ice between ∼50–60°N, and ice is stable at depths ranging from 1 cm to 2 m in the Tharsis region. The reduced areal extent of ice in the northern hemisphere is because the increased obliquity results in both warmer mean annual surface temperatures at these latitudes, and reduced mean annual near-surface atmospheric vapour pressures. The latter is caused by the warmer summertime temperatures increasing vapour transport away from the polar regions at higher altitudes, reducing the near-surface vapour values.

The stable ice over the Tharsis region is related to cloud formation. As the water cycle at $\varepsilon = 30°$ is wetter than in the present day, thick clouds form around the Tharsis Montes. Ice which sediments onto the surface at night sublimes during the day, increasing the near-surface vapour values compared to the surrounding areas, and allowing for the stability of subsurface ice. There is no stable subsurface ice in the mid-latitudes to the north of Alba Mons, unlike at $\varepsilon = 25.19°$. This is due to the warmer mean annual surface temperature and reduced mean annual near-surface atmospheric vapour pressure, as discussed earlier. As in the $\varepsilon = 15°$ simulations, the regions of stable ice in the tropics and mid-latitudes are not present in the simulations with a clear atmosphere or with zero eccentricity. Thus, when determining to what depth ice may be stable, particularly away from the polar regions, it is important to consider the circulation and dustiness of the atmosphere, along with cloud formation, as these can have a large effect on the near-surface vapour values.

At $\varepsilon = 31.1°$, Mellon and Jakosky (1995) predicted subsurface ice to be stable to depths of a few centimetres over almost the whole globe, while at $\varepsilon = 30°$, Chamberlain and Boynton (2007) predicted no stable subsurface ice between around 15°N–35°S. Chamberlain and Boynton (2007) noted that they predicted less extensive subsurface ice deposits due to (i) their smaller global vapour column value of 100 pr-μm, compared to 232 pr-μm in Mellon and Jakosky (1995), and (ii) their use of a near-surface vapour depletion scheme. Our results in Figure 8c show less extensive stable subsurface ice deposits than predicted by Mellon and Jakosky (1995), as we have smaller vapour columns in our simulations. Compared to Chamberlain and Boynton (2007), our results show a reduction in the amount of stable subsurface ice in the northern hemisphere mid-latitudes, which is also likely due to the

smaller vapour columns in our simulations. We also predict extensive stable subsurface ice in the Tharsis region, unlike Chamberlain and Boynton (2007), which is related to cloud formation as discussed earlier.

6. Regolith-atmosphere interaction between 5–20 Mya

Throughout the time period 5–20 Mya, Mars' obliquity ranged from around 25–45° (Laskar et al., 2004, and see also Figure 1). As we have already studied the regolith-atmosphere interaction at $\varepsilon = 30°$, here we concentrate on $\varepsilon = 45°$. Again we vary L_p, e and τ_vis, but we also consider two distinct surface ice reservoirs: polar ice caps and tropical ice reservoirs. This is because while ice caps are likely to remain at the poles as Mars approaches $\varepsilon = 45°$, previous modelling work has shown that at this obliquity stable ice forms at tropical latitudes (e.g. Mischna et al., 2003; Forget et al., 2006). The polar ice caps are again defined at the pole which experiences summer during aphelion (or at the north pole for simulations with a circular orbit). The tropical ice reservoir is placed in the Tharsis region between 100°–125°W and 22°N–22°S (two grid points at T5 resolution; see Figure 2).

6.1. Polar ice reservoirs

Considering first the simulations with polar ice caps, there is a large difference in water abundances between the clear and dusty simulations (see Figure 4c). The increased atmospheric temperatures in the dusty simulations act to transport more water away from the ice caps, allowing more ice to sublime. This results in a water cycle that is globally wetter than for a clear atmosphere, with peak vapour columns of around 1500 pr-μm over the subliming ice caps and 200 pr-μm in the tropics. Additionally, the lower daytime surface temperatures in the dusty simulations limit the amount of vapour diffusing back out of the regolith. Thus, both surface and subsurface ice forms much more extensively in the dusty simulations.

In the clear simulations, subsurface ice forms at the opposite pole to that where the ice cap was defined (initially at a depth of $\sim$1 m), though the values after 820 years (800 years at T5 resolution and 20 years at T31 resolution) are only small ($\sim$2 kg m^{-2}). In the dusty simulations the ice is not limited to the polar regions, and exists at all latitudes, though not all longitudes (see Figure 9). Ice is nearest to the surface in the Tharsis region, with the top of the ice layer varying between 2–5 cm, depending on location. In the polar regions, ice is stable at depths between around 0.1–1 m (here, ice stability is

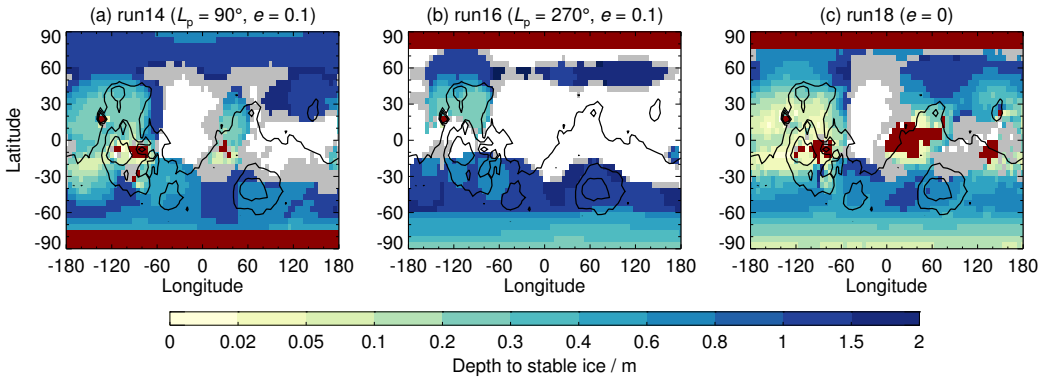

Figure 9: Depth to stable subsurface ice deposits for the three dusty simulations at $\varepsilon = 45°$. Red shading at the poles denotes the locations of the specified ice caps, while red shading away from the poles denotes the locations where stable surface ice with a depth >1 cm has formed in the simulations. Grey shading shows locations where there is seasonal subsurface ice but no stable ice. White shading shows locations where there is no subsurface ice at any time throughout the year. Results are after 820 years of simulation (800 years at T5 resolution and 20 years at T31 resolution), not from an equilibrium ice table depth calculation. Black contours show topography.

determined from the diffusion/condensation model, not the equilibrium ice table depth model). In all simulations at $\varepsilon = 45°$, regions centred around 30°W and 100°E are free of stable subsurface ice due to the combination of higher regolith thermal inertia and the atmospheric circulation transporting less water to these regions. These results are similar to those of Jakosky et al. (2005) when they assumed an atmospheric water content of 100 pr-μm, hypothesised to result from the southern ice cap losing its CO_2 covering relatively recently, allowing more water to sublime.

The results from the clear simulations at $\varepsilon = 45°$ are in agreement with those of Chamberlain and Boynton (2007), who found that subsurface ice is not stable close to the equator at $\varepsilon = 45°$. However, the dusty simulation results, with stable subsurface ice at various locations in the tropics, fall between those of Chamberlain and Boynton (2007) and those of Mellon and Jakosky (1995), who found that subsurface ice is stable everywhere at $\varepsilon > 32°$. The reason for the increased abundance of subsurface ice compared to Chamberlain and Boynton (2007) is likely because the vapour columns in the tropics in our simulations are larger ($\sim$200 pr-μm compared to $\sim$100 pr-μm). Thus, in order to fully understand the location and stability of subsurface

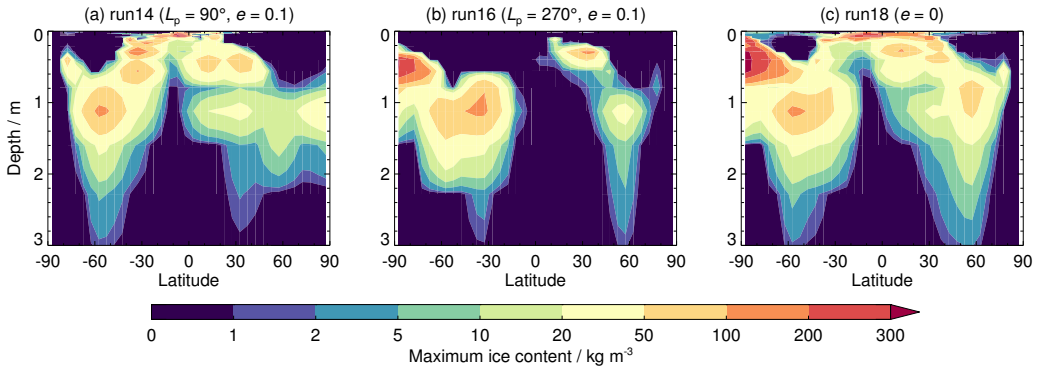

Figure 10: The maximum ice concentration around each latitude circle, as a function of latitude and depth, for three dusty simulations at $\varepsilon = 45°$. Results are from year 820 (with 800 years at T5 resolution and 20 years at T31 resolution). Ice caps were defined at the south pole in run14 and the north pole in run16 and run18.

ice during past epochs, it is clear that we need an understanding of the dust and water cycles, in particular how the atmospheric circulation affects the near-surface vapour distribution.

While Figure 9 shows the depth to the top of the ice layer, Figure 10 shows the range of depths subsurface ice exists over, in terms of the maximum ice concentrations as a function of latitude and depth. While this is a snapshot of the ice distribution after 820 years, with ice abundances still increasing, it highlights the spatial heterogeneity of the ice deposition. In the mid-latitudes, ice occurs at depths ranging from around 0.5–2.5 m, and, as the poles are approached, the range of depths decreases and the ice exists closer to the surface. In the tropics there is a large variation in ice depth, varying between 1 cm and 2.5 m. This is due to the variation in topography encountered, as well as variations in soil properties and vapour amounts. Subsurface ice does not exist as close to the surface in run16 (Figure 10b), as the orbital parameters result in lower vapour abundances, and hence not enough vapour diffuses into the regolith to exceed the saturation value in the relatively warm tropics. Subsurface ice amounts in the tropics peak at around 50–100 kg m^{-3} depending on the simulation. Larger subsurface ice amounts form in the polar regions, becoming almost pore-filling in the southern polar region in run18 (Figure 10c). These large ice values decrease the porosity of the regolith (which falls to around 0.07 for 300 kg m^{-3} of ice), reducing the

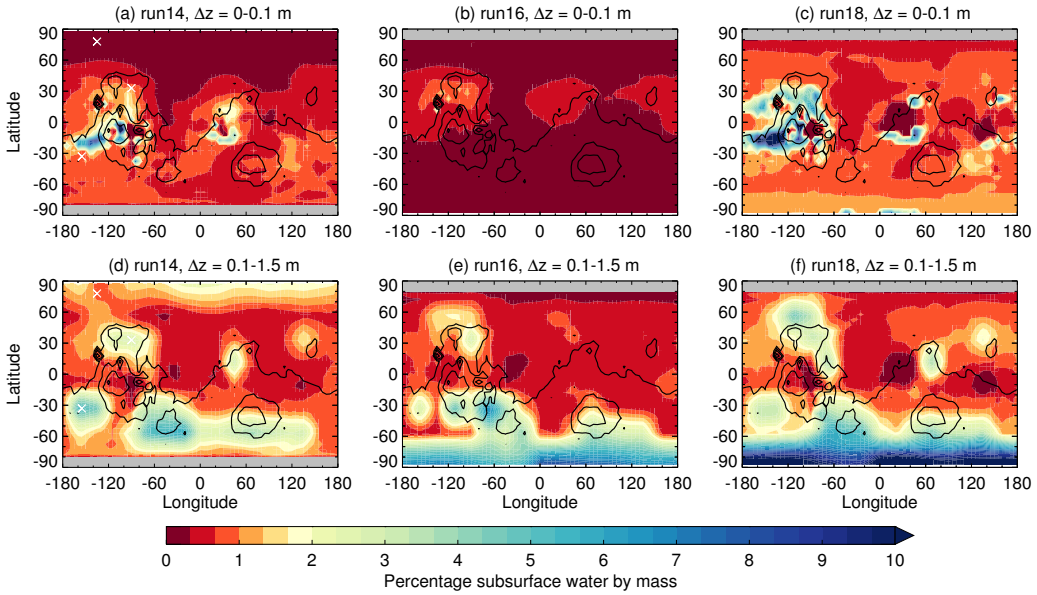

Figure 11: Total subsurface water content (adsorbed water, ice and vapour) over (a–c) the upper 10 cm of regolith, and (d–f) the 10 cm–1.5 m depth range, after 820 years of simulation (800 years at T5 resolution and 20 years at T31 resolution). Results are shown for (a,d) run14, (b,e) run16, and (d,f) run18. Polar ice cap locations are shown with grey shading. Black contours show topography, and white crosses in panels (a,d) show the locations of the 1D simulations in Figure 12.

diffusion coefficient and limiting the transport of vapour below the ice layer.

In terms of the spatial distribution of subsurface water (not just ice) at high obliquity, Figure 11 shows the global subsurface water content from three simulations (run14, run16 and run18) in the top 10 cm of regolith (upper panels) and between 10 cm–1.5 m (lower panels). The water content is given as a percentage of the total mass, i.e. $\mathrm{wt}\% = 100\sigma/(\sigma + \rho_{\mathrm{reg}})$. It can be seen that the subsurface water distributions are different over the two depth ranges considered. In the upper 10 cm, run14 and run18 (panels a,c) have increased water abundances in the Tharsis region and Arabia Terra, while run18 also has increased water around Elysium Mons and on the dichotomy boundary between Elysium Planitia and Terra Cimmeria (centred around 20°S, 150°E). These locations correspond to areas surrounding stable surface ice deposits (see Figure 9) where the atmospheric water content is large at times when the surface ice is subliming. Little stable surface ice was deposited in run16,

hence the upper 10 cm of regolith are relatively dry (panel b).

Lower down in the regolith, between 0.1–1.5 m, subsurface ice forms at the pole opposite that where the ice cap was defined. Thus, run14 has subsurface ice at the north pole, while run16 and run18 have subsurface ice at the south pole (Figure 11, panels d–f). Ice amounts are larger in run16 and run18 (up to ∼15% water by mass) compared to run14 (< 5% water by mass), as the peak atmospheric vapour abundances are larger (∼1000 pr-μm compared to ∼500 pr-μm). Away from the polar regions, all three simulations show relative increases in water to the north and south-west of the Tharsis region, and around the Argyre and Hellas basins. This is because these regions experience increased atmospheric water content due to transport by topographically-steered flows around Tharsis, and stationary waves around the Argyre and Hellas basins. Peak vapour columns range from 500–1000 pr-μm in run14, and 500–2000 pr-μm in run16 and run18. Additionally, run14 and run18 have increased subsurface water around Arabia Terra (resulting from diffusion close to the stable surface ice deposits) and to the north-west of Elysium Mons.

Compared to the results from $\varepsilon = 30°$ (Figure 6) it can be seen that the $\varepsilon = 45°$ results are quite different. The reasons for these differences are partly due to circulation changes at high obliquity, which result in a vapour distribution different to that at lower obliquity, but are also due to the increased water abundances. This means that saturation can be reached and ice can form even in regions where the subsurface temperatures are relatively warm. Also, the formation of stable surface ice in various locations can lead to the surrounding regions having relatively large values of subsurface water. Thus, while regolith properties strongly determine the subsurface water distribution in the present day and at $\varepsilon = 30°$, they have less of an impact at high obliquity when the vapour abundance is larger.

As these results are after only 820 years of simulation, we chose three locations from run14 to perform further one-dimensional simulations for 50 kyr, as we did for the $\varepsilon = 30°$ case. We chose one location in the north polar region (78°N, 135°W), one to the east of Alba Mons (33°N, 90°W) and one to the south west of the Tharsis region (33°S, 155°W), in order to obtain a variety of different conditions. The results are shown in Figure 12. The simulation in Figure 12c uses a time step of 30 s (as opposed to 1 minute at the other locations), as the large near-surface vapour values, and the long period of time diffusion is occurring over (see Figure 12d), can cause numerical instabilities with longer time steps.

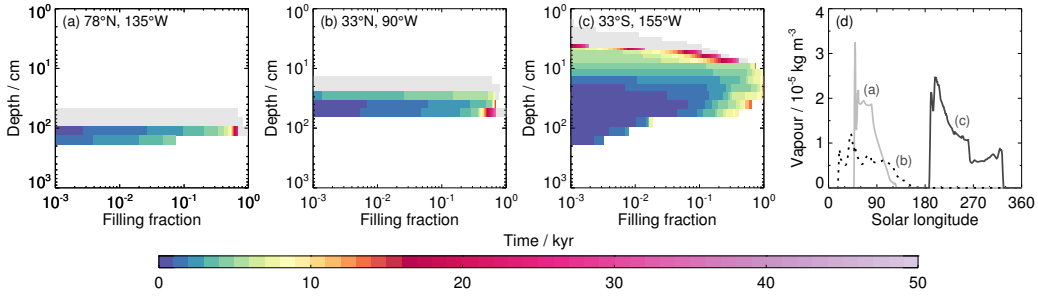

Figure 12: Variation of (a–c) the filling fraction, and (d) the near surface water abundance as in Figure 7, but for three locations at $\varepsilon = 45°$.

Stable ice in the north polar region (Figure 12a) exists deeper in the regolith than at the other two locations. This is because the high obliquity results in warmer peak subsurface temperatures. For example, at a depth of 30 cm, peak temperatures at 78°N are ∼255 K, compared to ∼210 K at the other two locations. Subsurface temperatures are similar at 33°N and 33°S, but near-surface vapour abundances are larger at 33°S (average value of 11.4 mg m^{-3} compared to 4.6 mg m^{-3} at 33°N), and so ice is more extensive and exists closer to the surface. Similar one-dimensional simulations were also performed for the corresponding clear simulation (run13) but the results are not shown as no subsurface ice formed, except at 33°N, where the results are the same as in Figure 12b.

After 50 kyr, the top of the ice table ranges from a depth of ∼90 cm at 78°N to ∼4 cm at 33°S. As for the $\varepsilon = 30°$ case, to see to what depth ice would be stable given a longer period of time, we filled the regolith with ice from the surface down to the layer with the largest ice abundance, and ran the simulations until the ice distribution reached equilibrium. The results are shown by the grey shading in Figure 12. As can be seen, the top of the ice table ranges from ∼50 cm at 78°N to ∼2 cm at 33°S. The stability depth of ice at 78°N is greater than at $\varepsilon = 30°$, where it was stable at ∼20 cm (see Figure 7a). This is because the subsurface temperatures in the polar region are warmer at high obliquity.

6.2. Tropical ice reservoir

As in the previous results with polar ice caps, dusty simulations, with a tropical ice reservoir acting as an unlimited source of water, result in in-

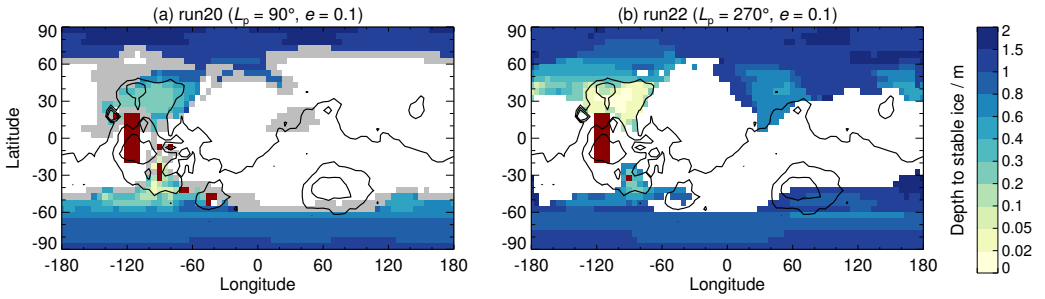

Figure 13: Depth to stable subsurface ice deposits for two dusty simulations at $\varepsilon = 45°$, with an ice reservoir defined in the Tharsis region (red rectangle). Red shading elsewhere denotes the locations where stable surface ice with a depth >1 cm has formed in the simulations. Grey shading shows locations where there is seasonal subsurface ice but no stable ice. White shading shows locations where there is no subsurface ice at any time throughout the year. Results are after 820 years of simulation (800 years at T5 resolution and 20 years at T31 resolution), not from an equilibrium ice table depth calculation. Black contours show topography.

creased formation of subsurface ice. Figure 13 shows the depth to stable subsurface ice for two dusty simulations after 820 years of simulation (the results of run24 are similar to run22). It can be seen that stable subsurface ice forms in both polar regions, initially at depths below ∼1 m. However, with time this ice moves closer to the surface as in Figure 12a. Stable subsurface ice close to the surface is found around Tempe Terra and Alba Mons (centred ∼30°N) and around Solis Planum and Argyre Planitia (centred ∼40°S). This is a result of the transport of large vapour values from the nearby Tharsis ice sheet, with vapour columns in the region reaching peak values of around 1000 pr-μm (annual mean values are around 30–100 pr-μm; see Figure 4d). As this transport is mainly meridional rather than zonal, the majority of the tropics are free of stable subsurface ice. Stable surface ice deposits also build up, which are shaded red. In Figure 13a these exist in similar regions to those in Figure 9(a,c), i.e. around the Tharsis region. Due to the large vapour values caused by the subliming Tharsis ice sheet, ice is accumulating at a rate of $\sim 1\,\mathrm{m\,yr^{-1}}$ over Olympus Mons, but around 0.01–0.2 $\mathrm{m\,yr^{-1}}$ at the other locations. In Figure 13b there is only one stable surface ice deposit away from the Tharsis ice sheet, located at around 30°S, 90°W. This reduction in stable surface ice is due to the warmer summertime temperatures.

7. Discussion

We find that the subsurface water content is affected by both the properties of the regolith (thermal inertia and albedo) and the atmospheric transport of vapour, with the relative importance of each depending upon the orbital parameters. At low to moderate obliquities ($\varepsilon = 15°$–$30°$), the regolith properties have more control on the subsurface water distribution in the tropics and mid-latitudes than changes to the eccentricity, e or solar longitude of perihelion, L_p. This is because changes to e and L_p only have a small effect on the amount of water sublimed from the polar ice cap, and as such the atmospheric water content remains relatively low (compared to at high obliquity). Thus, the amount of water diffused into the regolith in the tropics and mid-latitudes is not large enough to reach saturation and form ice, so the water exists mostly in its adsorbed state. The amount of adsorbed water decreases as temperatures increase (as the water is mobilised into vapour which then diffuses out of the regolith), so low thermal inertia regions (which have greater day-night temperature variability but lower mean temperatures) tend to have locally higher subsurface water contents. Conversely, at high obliquity ($\varepsilon = 45°$) atmospheric vapour abundances become much larger, and more vapour can diffuse further into the regolith, allowing subsurface ice to form at all latitudes (but not all longitudes).

Compared to observations of the present-day global subsurface water distribution by the MONS instrument (Feldman et al., 2004, 2007, 2008; Maurice et al., 2011), the simulations for $\varepsilon = 30°$ with a north polar ice cap show the best agreement. This suggests the subsurface water distribution revealed by MONS is likely to occur for a range of obliquities close to that of today, when the atmospheric water content is supplied by a north polar ice cap. The circulation of the atmosphere is also important in producing the observed subsurface water distribution. The MONS observations of increased subsurface water abundances and decreased burial depths centred roughly at 135°W, 70°N and 90°E, 70°S (Feldman et al., 2007; Maurice et al., 2011) are the result of increased atmospheric water content due to transport by topographically-steered flows to the west of Tharsis during northern hemisphere summer, and stationary waves to the east of Hellas during southern hemisphere summer. As these circulation patterns are due to topographic features, it is likely the same regions will also experience increased subsurface water at different obliquities, and shows the importance of considering the effect of the atmospheric circulation on the near-surface vapour values.

While there is agreement with the spatial distribution of subsurface water, our model results at $\varepsilon = 30°$ tend to have lower water masses than observed by MONS. One reason for this may be the choice of adsorption isotherm, with the amount of water adsorbed differing by a factor of ∼100 between different isotherms (Zent and Quinn, 1997). In the polar regions, a match to the MONS measurements of ∼60% water by weight would only be possible if the regolith porosity was ∼80%, with all the pore space being filled with ice. However, this is larger than the porosity determined at the Viking Lander 1 site (Moore and Jakosky, 1989; Boynton et al., 2002), and larger than the maximum predicted porosity of 65% (Prettyman et al., 2004). A more likely reason for the large water values observed by MONS in the polar regions would be the combination of pore ice from vapour diffusion along with ice lenses (Sizemore et al., 2015) or buried surface ice (Jakosky and Carr, 1985; Mischna et al., 2003; Levrard et al., 2004). In the equatorial region, the high water-equivalent hydrogen abundances of ∼10% by weight (which cannot be matched by the GCM) are likely due to the presence of hydrous minerals (e.g. Bish et al., 2003; Wang et al., 2013; Karunatillake et al., 2014). Our drier regolith is also likely related to the fact that our GCM simulations have run for only ∼800 years, and diffusion of significant amounts of water is a relatively slow process (the additional one-dimensional simulations show that large amounts of pore ice can accumulate over thousands of years in various locations).

While subsurface ice in the tropics and mid-latitudes did not form in our simulations at $\varepsilon = 15°$, and only formed over the polar regions at $\varepsilon = 30°$, we can use the near-surface vapour values and regolith temperatures to determine the equilibrium ice table depth. At $\varepsilon = 15°$ we predict stable subsurface ice in the region around Olympus Mons and Alba Mons, while none was predicted in previous studies by Mellon and Jakosky (1995) and Chamberlain and Boynton (2007). This difference is likely related to the vapour values used, as Mellon and Jakosky (1995) assumed a value of 2.62 pr-μm and Chamberlain and Boynton (2007) assumed a value of 0.33 pr-μm, while our simulations have values of ∼15 pr-μm. At $\varepsilon = 30°$ we predict less extensive stable subsurface ice deposits than Mellon and Jakosky (1995), as we have lower vapour columns in our simulations of ∼60–80 pr-μm (compared to 232 pr-μm). We also predict stable subsurface ice in the Tharsis region, while Chamberlain and Boynton (2007) do not. This is because the near-surface vapour values in the Tharsis region are increased due to the sedimentation (and subsequent sublimation) of ice particles from the thick clouds which

form. Thus, it is important to consider the atmospheric circulation when determining to what depth ice may be stable, particularly away from the polar regions, as this can have a large effect on the near-surface vapour values

At $\varepsilon = 45°$, subsurface ice forms only in the polar regions in the clear simulations, while in the dusty simulations a large amount of stable subsurface ice exists at all latitudes (though not all longitudes). When polar ice caps are defined, the subsurface ice is extensive around the Tharsis region, and around Arabia Terra and north of Elysium. When an ice reservoir is instead defined over the Tharsis Montes, subsurface ice is much less abundant in the tropics, and exists mainly to the north and south of the ice reservoir (as the circulation preferentially transports the sublimed vapour meridionally rather than zonally). Indeed, in all simulations a dusty atmosphere leads to increased subsurface water contents compared to a clear atmosphere. There are two reasons for this. Firstly, the dustier atmosphere is warmer and acts to transport more water away from the subliming ice reservoirs. Secondly, the dusty simulations have lower daytime surface temperatures, so less of the adsorbed water diffuses back into the atmosphere, and vapour can reach saturation as regolith temperatures are lower. As shown by Newman et al. (2005), dust lifting by both near-surface wind stress and dust devils increases with increasing obliquity, so Mars at high obliquity was likely dustier than it is today. Thus it is important to gain a better understanding of the dust cycle at past epochs, as it has a large effect on subsurface ice stability.

It should be noted that the simulations performed here do not include the radiative impact of clouds. Recent modelling and data assimilation studies have shown that clouds in the present-day can influence the temperature structure of the atmosphere and strengthen the overturning circulation (e.g. Wilson et al., 2008; Madeleine et al., 2012; Steele et al., 2014a; Navarro et al., 2014), potentially bringing modelling results into better agreement with observations. Madeleine et al. (2014) have also shown that, at 35° obliquity, cloud radiative effects can increase the atmospheric vapour content by more than an order of magnitude. The effect is similar to that in our dusty simulations, in which increased atmospheric temperatures strengthen the meridional circulation and allow more vapour to be transported away from the subliming polar ice caps in the summer. We chose not to include cloud radiative effects in our simulations for a number of reasons. Firstly, the GCM was run at a low resolution with grid boxes of 22.5°, to enable many hundreds of years to be simulated. As such, the horizontal extent of any clouds in the tropics will be larger than would occur in reality, which will

affect the scale of any heating/cooling. Secondly, there is a complex coupling between the dust and water cycles, and here we are only considering either clear or dusty conditions, and not transporting dust particles (again, because of the low resolution of the GCM, but also due to a lack of knowledge of the dust cycle in past epochs). Thirdly, while cloud radiative effects have led to improvements in model predictions of the present-day climate, they also lead to some inconsistencies (e.g. Madeleine et al., 2012; Navarro et al., 2014), and for past epochs we cannot check with observations to see which features are likely correct or incorrect. Thus, we note that it is possible that in reality the water cycle may have been wetter than represented in our $\varepsilon = 45°$ simulations, which would result in larger subsurface ice values than predicted, and possibly increased rates of surface ice accumulation in the tropics.

8. Conclusions

We have used a GCM with a regolith diffusion model in order to study the regolith-atmosphere exchange of vapour in Mars' recent past. We have run GCM simulations for hundreds of years, and one-dimensional simulations for thousands of years, and considered various orbital parameters (obliquity, eccentricity and the solar longitude of perihelion), atmospheric dust contents and surface ice reservoirs. Our main findings are as follows:

1. It is important to consider the circulation of the atmosphere when determining the subsurface water distribution. The simulations performed here show that circulation patterns forced by topography lead to increased near-surface (and hence increased subsurface) water abundances in regions where MONS observations show increased subsurface water abundances and decreased burial depths. Due to the nature of the topographic forcing, it is likely the same regions will also have experienced increased subsurface water in the past, and will do so in the future.
2. The dustiness of the atmosphere plays an important role in the distribution of subsurface water. As the dustiness increases, the warmer atmospheric temperatures allow more water to sublime and be transported away from surface ice deposits. The colder surface temperatures in a dusty atmosphere mean subsurface ice can be stable closer to the surface and closer to the equator, particularly at high obliquity where atmospheric humidities can be very large. Newman et al. (2005) showed

an increase in dust lifting with increasing obliquity, so Mars at high obliquity was likely dustier than it is today, and extensive subsurface ice may have been prevalent.

3. At $\varepsilon = 45°$, large regions of stable subsurface ice form in the midlatitudes and tropics when a permanent polar ice cap is defined. However, when defining a tropical ice sheet in the Tharsis region instead, the majority of the tropics are free of stable subsurface ice. This is because the atmospheric circulation preferentially transports the subliming vapour away from the ice sheet meridionally rather than zonally.

Appendix A. Regolith diffusion model

The one-dimensional diffusion calculation operates on the water vapour plus adsorbed water component of each grid box, e.g. on $m = \phi n + \alpha$ (see Equation 1). The regolith scheme thus solves the equation

$$\frac{\delta m}{\delta t} = \frac{\delta J}{\delta z}, \tag{A.1}$$

with $J = D\delta n/\delta z$, where δz is the depth below the surface.

Adsorption of water vapour onto regolith grains uses an empirical relation from Fanale and Cannon (1971):

$$\alpha(n, T) = \frac{\rho_\mathrm{r}\beta\sqrt{n}}{e^{\delta/T}}\left(\frac{k_\mathrm{B}T}{m_\mathrm{w}}\right)^{0.51} = F(T)\sqrt{n}, \tag{A.2}$$

where ρ_r is the regolith density, $\beta = 2.043 \times 10^{-8}$ Pa^{-1}, $\delta = -2679.8$ K, T is the temperature, k_B is the Boltzmann constant and m_w is the mass of a water molecule. Thus, at time t in regolith layer k we have $m_k^t = \phi_k^t n_k^t + F(T_k^t)\sqrt{n_k^t} = \phi_k^t n_k^t + F_k^t\sqrt{n_k^t}$. Solving for n_k^t gives

$$n_k^t = \frac{{m_k^t}^2}{F_k^{t2}}\left(1 - \frac{2m_k^t\phi_k^t}{F_k^{t2}}\right). \tag{A.3}$$

If ice is present, Equation A.3 will result in $n_k^t = n_\mathrm{sat}$. Equation A.3 is used to obtain a relation for the vapour increment:

$$\begin{aligned}\delta n_k^t &= n_k^t - n_k^{t-dt} \\ &= \frac{{m_k^t}^2}{F_k^{t2}}\left(1 - \frac{2m_k^t\phi_k^t}{F_k^{t2}}\right) - \frac{{m_k^{t-dt}}^2}{F_k^{t-dt2}}\left(1 - \frac{2m_k^{t-dt}\phi_k^{t-dt}}{F_k^{t-dt2}}\right).\end{aligned} \tag{A.4}$$

To remove the dependence of Equation A.4 on m_k^t, we substitute in $m_k^t = m_k^{t-dt} + \delta m_k^t$, and ignore terms with powers of δm_k^t (since $\delta m_k^t \ll m_k^t$). This results in the equation $\delta n_k^t = A_k^t \delta m_k^t + B_k^t$, where

$$A_k^t = \frac{2m_k^{t-dt}}{{F_k^t}^2} - \frac{6{m_k^{t-dt}}^2 \phi_k^{t-dt}}{{F_k^t}^4} \tag{A.5}$$

and

$$B_k^t = \left(\frac{1}{{F_k^t}^2} - \frac{1}{{F_k^{t-dt}}^2}\right) {m_k^{t-dt}}^2 - 2\phi_k^{t-dt} \left(\frac{1}{{F_k^t}^4} - \frac{1}{{F_k^{t-dt}}^4}\right) {m_k^{t-dt}}^3. \tag{A.6}$$

Thus, we have

$$\frac{\delta m_k^t}{\delta t} = \frac{\delta n_k^t - B_k^t}{A_k^t \delta t}, \tag{A.7}$$

and hence Equation A.1 becomes

$$\frac{n_k^t - n_k^{t-dt} - B_k^t}{A_k^t \delta t} = \frac{J_{k+0.5}^t - J_{k-0.5}^t}{z_{k+0.5} - z_{k-0.5}}, \tag{A.8}$$

where

$$J_{k+0.5}^t = D_{k+0.5}^t \frac{n_{k+1}^t - n_k^t}{z_{k+1} - z_k}. \tag{A.9}$$

The $k \pm 1$ subscripts denote terms evaluated at layer midpoints, with the $k \pm 0.5$ terms evaluated at layer boundaries. Combining Equations A.8 and A.9 gives

$$C_k^t (n_k^{t-dt} + B_k^t) = \Pi_k^t n_k^t - d_{k-0.5}^t n_{k-1}^t - d_{k+0.5}^t n_{k+1}^t, \tag{A.10}$$

where

$$\begin{aligned} C_k^t &= (z_{k+0.5} - z_{k-0.5}) / A_k^t \delta t, \\ \Pi_k^t &= C_k^t + d_{k-0.5}^t + d_{k+0.5}^t, \\ d_{k+0.5}^t &= D_{k+0.5}^t / (z_{k+1} - z_k). \end{aligned}$$

We require a solution to Equation A.10 of the form $n_k^t = \gamma_{k-0.5}^t n_{k-1}^t + \beta_{k-0.5}^t$. Thus, in order to remove the n_{k+1}^t term from Equation A.10, we

substitute with $n^t_{k+1} = \gamma^t_{k+0.5} n^t_k + \beta^t_{k+0.5}$. This results in

$$n^t_k = \left(\frac{d^t_{k-0.5}}{\Pi^t_k - d^t_{k+0.5}\gamma^t_{k+0.5}} \right) n^t_{k-1} + \frac{C^t_k \left(n^{t-dt}_k + B^t_k \right) + d_{k+0.5}\beta^t_{k+0.5}}{\Pi^t_k - d^t_{k+0.5}\gamma^t_{k+0.5}}$$

$$= \gamma^t_{k-0.5} n^t_{k-1} + \beta^t_{k-0.5}. \tag{A.11}$$

Once n^t_k has been calculated for each regolith layer using Equation A.11, the increments $\delta n^t_k = n^t_k - n^{t-dt}_k$ are calculated, leading to the new total water content $\sigma^t_k = \sigma^{t-dt}_k + (\delta n^t_k - B^t_k)/A^t_k$. Once σ^t_k is known, partitioning of the water content into the three states is carried out. If $n^t_k \leq n_{\rm sat}$ (with n^t_k calculated from Equation A.3, though now using the total water content, σ^t_k, rather than the ice-free content m^t_k) then $\alpha^t_k = F(T^t_k)\sqrt{n^t_k}$ and $\zeta^t_k = 0$. If $n_t > n_{\rm sat}$ then $n^t_k = n_{\rm sat}$, $\alpha^t_k = F(T^t_k)\sqrt{n_{\rm sat}}$ and $\zeta^t_k = \sigma^t_k - \phi^t_k n_{\rm sat} - F(T^t_k)\sqrt{n_{\rm sat}}$. Thus, the diffusion calculation uses the ice-free water content in each grid box to calculate the vapour flux. This is to avoid unrealistically large values of the A^t_k and B^t_k coefficients, which would result from large values of σ^t_k. The vapour change in each grid box is then added to the previous time step's total water content, and this is used in the condensation-sublimation step.

Acknowledgements

This work was funded by the UK Science and Technology Facilities Council, grant number ST/L000776/1. The authors thank Hanna Sizemore, Pierre-Yves Meslin and two anonymous reviewers, whose comments helped improve this paper.

References

Aharonson, O., Schorghofer, N., 2006. Subsurface ice on Mars with rough topography. J. Geophys. Res. (Planets) 111, E11007.

Arvidson, R. E., Bonitz, R. G., Robinson, M. L., Carsten, J. L., Volpe, R. A., Trebi-Ollennu, A., Mellon, M. T., Chu, P. C., Davis, K. R., Wilson, J. J., Shaw, A. S., Greenberger, R. N., Siebach, K. L., Stein, T. C., Cull, S. C., Goetz, W., Morris, R. V., Ming, D. W., Keller, H. U., Lemmon, M. T., Sizemore, H. G., Mehta, M., 2009. Results from the Mars Phoenix Lander Robotic Arm experiment. J. Geophys. Res. (Planets) 114.

Beck, P., Pommerol, A., Schmitt, B., Brissaud, O., 2010. Kinetics of water adsorption on minerals and the breathing of the Martian regolith. J. Geophys. Res. (Planets) 115.

Benson, J. L., Kass, D. M., Kleinböhl, A., 2011. Mars' north polar hood as observed by the Mars Climate Sounder. J. Geophys. Res. (Planets) 116, E03008.

Benson, J. L., Kass, D. M., Kleinböhl, A., McCleese, D. J., Schofield, J. T., Taylor, F. W., 2010. Mars' south polar hood as observed by the Mars Climate Sounder. J. Geophys. Res. (Planets) 115, E12015.

Bish, D. L., William Carey, J., Vaniman, D. T., Chipera, S. J., 2003. Stability of hydrous minerals on the martian surface. Icarus 164, 96–103.

Böttger, H. M., Lewis, S. R., Read, P. L., Forget, F., 2004. The effect of a global dust storm on simulations of the Martian water cycle. Geophys. Res. Lett. 31, L22702.

Böttger, H. M., Lewis, S. R., Read, P. L., Forget, F., 2005. The effects of the martian regolith on GCM water cycle simulations. Icarus 177, 174–189.

Boynton, W. V., Feldman, W. C., Squyres, S. W., Prettyman, T. H., Brückner, J., Evans, L. G., Reedy, R. C., Starr, R., Arnold, J. R., Drake, D. M., Englert, P. A. J., Metzger, A. E., Mitrofanov, I., Trombka, J. I., d'Uston, C., Wänke, H., Gasnault, O., Hamara, D. K., Janes, D. M., Marcialis, R. L., Maurice, S., Mikheeva, I., Taylor, G. J., Tokar, R., Shinohara, C., 2002. Distribution of Hydrogen in the Near Surface of Mars: Evidence for Subsurface Ice Deposits. Science 297, 81–85.

Bryson, K. L., Chevrier, V., Sears, D. W. G., Ulrich, R., 2008. Stability of ice on Mars and the water vapor diurnal cycle: Experimental study of the sublimation of ice through a fine-grained basaltic regolith. Icarus 196, 446–458.

Byrne, S., Dundas, C. M., Kennedy, M. R., Mellon, M. T., McEwen, A. S., Cull, S. C., Daubar, I. J., Shean, D. E., Seelos, K. D., Murchie, S. L., Cantor, B. A., Arvidson, R. E., Edgett, K. S., Reufer, A., Thomas, N., Harrison, T. N., Posiolova, L. V., Seelos, F. P., 2009. Distribution of Mid-Latitude Ground Ice on Mars from New Impact Craters. Science 325, 1674–
.

1011 Chamberlain, M. A., Boynton, W. V., 2007. Response of Martian ground ice
1012 to orbit-induced climate change. J. Geophys. Res. (Planets) 112.

1013 Chevrier, V., Ostrowski, D. R., Sears, D. W. G., 2008. Experimental study
1014 of the sublimation of ice through an unconsolidated clay layer: Implica-
1015 tions for the stability of ice on Mars and the possible diurnal variations in
1016 atmospheric water. Icarus 196, 459–476.

1017 Chevrier, V., Sears, D. W. G., Chittenden, J. D., Roe, L. A., Ulrich, R.,
1018 Bryson, K., Billingsley, L., Hanley, J., 2007. Sublimation rate of ice under
1019 simulated Mars conditions and the effect of layers of mock regolith JSC
1020 Mars-1. Geophys. Res. Lett. 34, 2203.

1021 Christensen, P. R., Bandfield, J. L., Hamilton, V. E., Ruff, S. W., Kieffer,
1022 H. H., Titus, T. N., Malin, M. C., Morris, R. V., Lane, M. D., Clark, R. L.,
1023 Jakosky, B. M., Mellon, M. T., Pearl, J. C., Conrath, B. J., Smith, M. D.,
1024 Clancy, R. T., Kuzmin, R. O., Roush, T., Mehall, G. L., Gorelick, N., Ben-
1025 der, K., Murray, K., Dason, S., Greene, E., Silverman, S., Greenfield, M.,
1026 2001. Mars Global Surveyor Thermal Emission Spectrometer experiment:
1027 Investigation description and surface science results. J. Geophys. Res. 106,
1028 23823–23872.

1029 Clifford, S. M., 1993. A model for the hydrologic and climatic behavior of
1030 water on Mars. J. Geophys. Res. 98, 10973.

1031 Cull, S., Arvidson, R. E., Mellon, M. T., Skemer, P., Shaw, A., Morris, R. V.,
1032 2010. Compositions of subsurface ices at the Mars Phoenix landing site.
1033 Geophys. Res. Lett. 37, L24203.

1034 Demidov, N. E., Bazilevskii, A. T., Kuz'min, R. O., 2015. Martian soils:
1035 Varieties, structure, composition, physical properties, drillability, and risks
1036 for landers. Solar Sys. Res. 49, 209–225.

1037 Evans, III, R. B., Watson, G. M., Mason, E. A., 1961. Gaseous Diffusion in
1038 Porous Media at Uniform Pressure. J. Chem. Phys. 35, 2076–2083.

1039 Fanale, F. P., Cannon, W. A., 1971. Adsorption on the Martian Regolith.
1040 Nature 230, 502–504.

1041 Fanale, F. P., Jakosky, B. M., 1982. Regolith-atmosphere exchange of water
1042 and carbon dioxide on Mars - Effects on atmospheric history and climate
1043 change. Planet. Space Sci. 30, 819–831.

1044 Fanale, F. P., Salvail, J. R., Zent, A. P., Postawko, S. E., 1986. Global
1045 distribution and migration of subsurface ice on Mars. Icarus 67, 1–18.

1046 Feldman, W. C., Bandfield, J. L., Diez, B., Elphic, R. C., Maurice, S., Nelli,
1047 S. M., 2008. North to south asymmetries in the water-equivalent hydrogen
1048 distribution at high latitudes on Mars. J. Geophys. Res. (Planets) 113.

1049 Feldman, W. C., Mellon, M. T., Gasnault, O., Diez, B., Elphic, R. C.,
1050 Hagerty, J. J., Lawrence, D. J., Maurice, S., Prettyman, T. H., 2007.
1051 Vertical distribution of hydrogen at high northern latitudes on Mars: The
1052 Mars Odyssey Neutron Spectrometer. Geophys. Res. Lett. 34.

1053 Feldman, W. C., Prettyman, T. H., Maurice, S., Nelli, S., Elphic, R., Fun-
1054 sten, H. O., Gasnault, O., Lawrence, D. J., Murphy, J. R., Tokar, R. L.,
1055 Vaniman, D. T., 2005. Topographic control of hydrogen deposits at low
1056 latitudes to midlatitudes of Mars. J. Geophys. Res. (Planets) 110.

1057 Feldman, W. C., Prettyman, T. H., Maurice, S., Plaut, J. J., Bish, D. L.,
1058 Vaniman, D. T., Mellon, M. T., Metzger, A. E., Squyres, S. W., Karunatil-
1059 lake, S., Boynton, W. V., Elphic, R. C., Funsten, H. O., Lawrence, D. J.,
1060 Tokar, R. L., 2004. Global distribution of near-surface hydrogen on Mars.
1061 J. Geophys. Res. (Planets) 109.

1062 Flasar, F. M., Goody, R. M., 1976. Diurnal behaviour of water on Mars.
1063 Planet. Space Sci., 161–181.

1064 Forget, F., Haberle, R. M., Montmessin, F., Levrard, B., Head, J. W.,
1065 2006. Formation of Glaciers on Mars by Atmospheric Precipitation at High
1066 Obliquity. Science 311, 368–371.

1067 Forget, F., Hourdin, F., Fournier, R., Hourdin, C., Talagrand, O., Collins,
1068 M., Lewis, S. R., Read, P. L., Huot, J.-P., 1999. Improved general circula-
1069 tion models of the Martian atmosphere from the surface to above 80 km.
1070 J. Geophys. Res. 104, 24155–24176.

1071 Hobbs, P. V., 1974. Ice physics. Oxford: Clarendon Press, 1974.

1072 Hudson, T., 2008. Growth, diffusion, and loss of subsurface ice on mars:
1073 experiments and models. Ph.D. Thesis, California Institute of Technology.

1074 Hudson, T. L., Aharonson, O., 2008. Diffusion barriers at Mars surface con-
1075 ditions: Salt crusts, particle size mixtures, and dust. J. Geophys. Res.
1076 (Planets) 113.

1077 Hudson, T. L., Aharonson, O., Schorghofer, N., 2009. Laboratory exper-
1078 iments and models of diffusive emplacement of ground ice on Mars. J.
1079 Geophys. Res. 114.

1080 Hudson, T. L., Aharonson, O., Schorghofer, N., Farmer, C. B., Hecht, M. H.,
1081 Bridges, N. T., 2007. Water vapor diffusion in Mars subsurface environ-
1082 ments. J. Geophys. Res. (Planets) 112, 5016.

1083 Jakosky, B. M., Carr, M. H., 1985. Possible precipitation of ice at low lati-
1084 tudes of Mars during periods of high obliquity. Nature 315, 559–561.

1085 Jakosky, B. M., Mellon, M. T., Varnes, E. S., Feldman, W. C., Boynton,
1086 W. V., Haberle, R. M., 2005. Mars low-latitude neutron distribution: Pos-
1087 sible remnant near-surface water ice and a mechanism for its recent em-
1088 placement. Icarus 175, 58–67.

1089 Kahre, M. A., Hollingsworth, J. L., Haberle, R. M., Wilson, R. J., 2015.
1090 Coupling the Mars dust and water cycles: The importance of radiative-
1091 dynamic feedbacks during northern hemisphere summer. Icarus 260, 477–
1092 480.

1093 Karunatillake, S., Wray, J. J., Gasnault, O., McLennan, S. M., Rogers, A. D.,
1094 Squyres, S. W., Boynton, W. V., Skok, J. R., Ojha, L., Olsen, N., 2014.
1095 Sulfates hydrating bulk soil in the Martian low and middle latitudes. Geo-
1096 phys. Res. Lett. 41, 7987–7996.

1097 Laskar, J., Correia, A. C. M., Gastineau, M., Joutel, F., Levrard, B., Robu-
1098 tel, P., 2004. Long term evolution and chaotic diffusion of the insolation
1099 quantities of Mars. Icarus 170, 343–364.

1100 Levrard, B., Forget, F., Montmessin, F., Laskar, J., 2004. Recent ice-rich de-
1101 posits formed at high latitudes on Mars by sublimation of unstable equa-
1102 torial ice during low obliquity. Nature 431, 1072–1075.

Lewis, S. R., Collins, M., Read, P. L., Forget, F., Hourdin, F., Fournier, R., Hourdin, C., Talagrand, O., Huot, J.-P., 1999. A climate database for Mars. J. Geophys. Res. 104, 24177–24194.

Lewis, S. R., Read, P. L., Conrath, B. J., Pearl, J. C., Smith, M. D., 2007. Assimilation of thermal emission spectrometer atmospheric data during the Mars Global Surveyor aerobraking period. Icarus 192, 327–347.

Määttänen, A., Listowski, C., Montmessin, F., Maltagliati, L., Reberac, A., Joly, L., Bertaux, J.-L., 2013. A complete climatology of the aerosol vertical distribution on Mars from MEx/SPICAM UV solar occultations. Icarus 223, 892–941.

Madeleine, J.-B., Forget, F., Head, J. W., Levrard, B., Montmessin, F., Millour, E., 2009. Amazonian northern mid-latitude glaciation on Mars: A proposed climate scenario. Icarus 203, 390–405.

Madeleine, J.-B., Forget, F., Millour, E., Navarro, T., Spiga, A., 2012. The influence of radiatively active water ice clouds on the Martian climate. Geophys. Res. Lett. 39.

Madeleine, J.-B., Head, J. W., Forget, F., Navarro, T., Millour, E., Spiga, A., Colaïtis, A., Määttänen, A., Montmessin, F., Dickson, J. L., 2014. Recent Ice Ages on Mars: The role of radiatively active clouds and cloud microphysics. Geophys. Res. Lett. 41, 4873–4879.

Mason, E., Malinauskas, A., 1983. Gas Transport in Porous Media: The Dusty-Gas Model. Vol. 17 of Chemical Engineering Monographs. Elsevier, Amsterdam.

Maurice, S., Feldman, W., Diez, B., Gasnault, O., Lawrence, D. J., Pathare, A., Prettyman, T., 2011. Mars Odyssey neutron data: 1. Data processing and models of water-equivalent-hydrogen distribution. J. Geophys. Res.(Planets) 116.

Mellon, M. T., Arvidson, R. E., Sizemore, H. G., Searls, M. L., Blaney, D. L., Cull, S., Hecht, M. H., Heet, T. L., Keller, H. U., Lemmon, M. T., Markiewicz, W. J., Ming, D. W., Morris, R. V., Pike, W. T., Zent, A. P., 2009. Ground ice at the Phoenix Landing Site: Stability state and origin. J. Geophys. Res. (Planets) 114.

Mellon, M. T., Feldman, W. C., Prettyman, T. H., 2004. The presence and stability of ground ice in the southern hemisphere of Mars. Icarus 169, 324–340.

Mellon, M. T., Jakosky, B. M., 1993. Geographic variations in the thermal and diffusive stability of ground ice on Mars. J. Geophys. Res. 98, 3345–3364.

Mellon, M. T., Jakosky, B. M., 1995. The distribution and behavior of Martian ground ice during past and present epochs. J. Geophys. Res. 100, 11781–11799.

Mellon, M. T., Jakosky, B. M., Kieffer, H. H., Christensen, P. R., 2000. High-Resolution Thermal Inertia Mapping from the Mars Global Surveyor Thermal Emission Spectrometer. Icarus 148, 437–455.

Mellon, M. T., Jakosky, B. M., Postawko, S. E., 1997. The persistence of equatorial ground ice on Mars. J. Geophys. Res. 102, 19357–19370.

Meslin, P.-Y., Gasnault, O., Forni, O., Schröder, S., Cousin, A., Berger, G., Clegg, S. M., Lasue, J., Maurice, S., Sautter, V., et al., 2013. Soil Diversity and Hydration as Observed by ChemCam at Gale Crater, Mars. Science 341.

Millington, R. J., 1959. Gas diffusion in porous media. Science 130 (3367), 100–102.

Mischna, M. A., Richardson, M. I., Wilson, R. J., McCleese, D. J., 2003. On the orbital forcing of Martian water and CO_2 cycles: A general circulation model study with simplified volatile schemes. J. Geophys. Res. (Planets) 108, 16–1.

Montabone, L., Forget, F., Millour, E., Wilson, R. J., Lewis, S. R., Cantor, B., Kass, D., Kleinböhl, A., Lemmon, M. T., Smith, M. D., Wolff, M. J., 2015. Eight-year climatology of dust optical depth on Mars. Icarus 251, 65–95.

Montmessin, F., Forget, F., Rannou, P., Cabane, M., Haberle, R. M., 2004. Origin and role of water ice clouds in the Martian water cycle as inferred from a general circulation model. J. Geophys. Res. (Planets) 109.

1166 Moore, H. J., Jakosky, B. M., 1989. Viking landing sites, remote-sensing
1167 observations, and physical properties of Martian surface materials. Icarus
1168 81, 164–184.

1169 Navarro, T., Madeleine, J.-B., Forget, F., Spiga, A., Millour, E., Montmessin,
1170 F., Määttänen, A., 2014. Global climate modeling of the Martian water
1171 cycle with improved microphysics and radiatively active water ice clouds.
1172 J. Geophys. Res. (Planets) 119, 1479–1495.

1173 Newman, C. E., Lewis, S. R., Read, P. L., 2005. The atmospheric circulation
1174 and dust activity in different orbital epochs on Mars. Icarus 174, 135–160.

1175 Piqueux, S., Christensen, P. R., 2009. A model of thermal conductivity for
1176 planetary soils: 2. Theory for cemented soils. J. Geophys. Res. (Planets)
1177 114.

1178 Pommerol, A., Schmitt, B., Beck, P., Brissaud, O., 2009. Water sorption on
1179 martian regolith analogs: Thermodynamics and near-infrared reflectance
1180 spectroscopy. Icarus 204, 114–136.

1181 Prettyman, T. H., Feldman, W. C., Mellon, M. T., McKinney, G. W., Boyn-
1182 ton, W. V., Karunatillake, S., Lawrence, D. J., Maurice, S., Metzger, A. E.,
1183 Murphy, J. R., Squyres, S. W., Starr, R. D., Tokar, R. L., 2004. Composi-
1184 tion and structure of the Martian surface at high southern latitudes from
1185 neutron spectroscopy. J. Geophys. Res. (Planets) 109.

1186 Schorghofer, N., 2007. Dynamics of ice ages on Mars. Nature 449, 192–194.

1187 Schorghofer, N., Aharonson, O., 2005. Stability and exchange of subsurface
1188 ice on Mars. J. Geophys. Res. (Planets) 110.

1189 Schorghofer, N., Forget, F., 2012. History and anatomy of subsurface ice on
1190 Mars. Icarus 220, 1112–1120.

1191 Siegler, M., Aharonson, O., Carey, E., Choukroun, M., Hudson, T.,
1192 Schorghofer, N., Xu, S., 2012. Measurements of thermal properties of icy
1193 Mars regolith analogs. J. Geophys. Res. (Planets) 117.

1194 Sizemore, H. G., Mellon, M. T., 2008. Laboratory characterization of the
1195 structural properties controlling dynamical gas transport in Mars-analog
1196 soils. Icarus 197, 606–620.

Sizemore, H. G., Zent, A. P., Rempel, A. W., 2015. Initiation and growth of martian ice lenses. Icarus 251, 191–210.

Smith, D. E., Zuber, M. T., Frey, H. V., Garvin, J. B., Head, J. W., Muhleman, D. O., Pettengill, G. H., Phillips, R. J., Solomon, S. C., Zwally, H. J., Banerdt, W. B., Duxbury, T. C., 1998. Topography of the Northern Hemisphere of Mars from the Mars Orbiter Laser Altimeter. Science 279, 1686.

Smith, M. D., 2004. Interannual variability in TES atmospheric observations of Mars during 1999-2003. Icarus 167, 148–165.

Smith, M. D., Wolff, M. J., Clancy, R. T., Kleinböhl, A., Murchie, S. L., 2013. Vertical distribution of dust and water ice aerosols from CRISM limb-geometry observations. J. Geophys. Res. (Planets) 118, 321–334.

Smoluchowski, R., 1968. Mars: Retention of Ice. Science 159, 1348–1350.

Steele, L. J., Lewis, S. R., Patel, M. R., 2014a. The radiative impact of water ice clouds from a reanalysis of Mars Climate Sounder data. Geophys. Res. Lett. 41, 4471–4478.

Steele, L. J., Lewis, S. R., Patel, M. R., Montmessin, F., Forget, F., Smith, M. D., 2014b. The seasonal cycle of water vapour on Mars from assimilation of Thermal Emission Spectrometer data. Icarus 237, 97–115.

Tokano, T., 2003. Spatial inhomogeneity of the martian subsurface water distribution: implication from a global water cycle model. Icarus 164, 50–78.

Vincendon, M., Forget, F., Mustard, J., 2010. Water ice at low to midlatitudes on Mars. J. Geophys. Res. (Planets) 115.

Wallace, D., Sagan, C., 1979. Evaporation of ice in planetary atmospheres - Ice-covered rivers on Mars. Icarus 39, 385–400.

Wang, A., Feldman, W. C., Mellon, M. T., Zheng, M., 2013. The preservation of subsurface sulfates with mid-to-high degree of hydration in equatorial regions on Mars. Icarus 226, 980–991.

Williams, K. E., McKay, C. P., Heldmann, J. L., 2015. Modeling the effects of martian surface frost on ice table depth. Icarus 261, 58–65.

Wilson, R. J., Lewis, S. R., Montabone, L., Smith, M. D., 2008. Influence of water ice clouds on Martian tropical atmospheric temperatures. Geophys. Res. Lett. 35, L07202.

Wilson, R. J., Neumann, G. A., Smith, M. D., 2007. Diurnal variation and radiative influence of Martian water ice clouds. Geophys. Res. Lett. 34, 2710.

Zalc, J. M., Reyes, S. C., Iglesia, E., 2004. The effects of diffusion mechanism and void structure on transport rates and tortuosity factors in complex porous structures. Chem. Eng. Sci. 59, 2947–2960.

Zent, A., 2008. A historical search for habitable ice at the Phoenix landing site. Icarus 196, 385–408.

Zent, A. P., Haberle, R. M., Houben, H. C., Jakosky, B. M., 1993. A coupled subsurface-boundary layer model of water on Mars. J. Geophys. Res. 98, 3319–3337.

Zent, A. P., Quinn, R. C., 1997. Measurement of H_2O adsorption under Mars-like conditions: Effects of adsorbent heterogeneity. J. Geophys. Res. 102, 9085–9096.

Zuber, M. T., Smith, D. E., Solomon, S. C., Muhleman, D. O., Head, J. W., Garvin, J. B., Abshire, J. B., Bufton, J. L., 1992. The Mars Observer laser altimeter investigation. J. Geophys. Res. 97, 7781–7797.